

Bronze-Phase TiO₂ as Anode Materials in Lithium and Sodium-Ion Batteries

Suzhe Liang, Xiaoyan Wang, Ruoxuan Qi, Ya-Jun Cheng,* Yonggao Xia, Peter Müller-Buschbaum,* and Xile Hu*

Titanium dioxide of bronze phase (TiO₂(B)) has attracted considerable attention as a promising alternative lithium/sodium-ion battery anode due to its excellent operation safety, good reversible capacity, and environmental friendliness. However, several intrinsic critical drawbacks, including moderate electrochemical kinetics and unsatisfactory long cyclic stability, significantly limit its practical applications. It is crucial to develop reliable strategies to resolve these issues to advance the TiO₂(B) based materials into practical applications in lithium/sodium-ion batteries. In this review, both the theoretical and experimental investigations on the TiO₂(B) based materials over the last few decades are chronically elaborated. Insights on the general and detailed evolution trends of the research on TiO₂(B) anodes are provided. The review also points to future directions for the TiO₂(B) anode research to advance the practical application of TiO₂(B) anodes.

long cycling life, minimum self-discharge, and limited memory effect. It has been a great success in the sense of both, technology and commercialization since it was first invented by Sony company in 1991.^[2] Graphite is used as anode in commercial LIBs, which offers satisfactory capacity and stable cycling life. However, it has a very low lithiation/delithiation potential, where excessive lithium plating and growth of lithium dendrite are possible during repeated charge/discharge processes.^[1] The uncontrolled lithium dendrite growth could penetrate the separator and thereby cause internal circuit short-cut and even explosion. Thus, the safety issue of the graphite anode has been one of the major concerns associated with the

1. Introduction

Lithium-ion batteries (LIBs) have been regarded as one of the most promising energy storage media, which have been widely used in different areas such as portable electronic devices, automotive vehicles, and smart grids.^[1] The LIB features various distinct advantages, including high energy density output,

LIB technology and it is essential to develop alternative LIB anodes to replace graphite.^[3–4]

Titanium dioxide (TiO₂) has been regarded as one of the most promising alternative anode materials for LIBs due to its better cycling stability compared to the up-to-the-moment alloying-type anode materials (such as silicon (Si), germanium (Ge), and tin (Sn)), abundance in nature, safety, and low costs.^[5–7]

S. Liang, P. Müller-Buschbaum
Lehrstuhl für Funktionelle Materialien
Physik-Department
Technische Universität München
James-Franck-Str. 1, 85748 Garching, Germany
E-mail: muellerb@ph.tum.de

X. Wang
School of Materials and Chemical Engineering
Ningbo University of Technology
201 Fenghua Road, Ningbo, Zhejiang 315211, P. R. China


X. Wang, R. Qi, Y.-J. Cheng, Y. Xia
Ningbo Institute of Materials Technology and Engineering
Chinese Academy of Sciences
1219 Zhongguan West Rd, Zhenhai
District, Ningbo, Zhejiang Province 315201, P. R. China
E-mail: chengyj@nimte.ac.cn

R. Qi
School of Materials Science and Engineering
Shanghai University
Shanghai 200444, P. R. China

Y. Xia
Center of Materials Science and Optoelectronics Engineering
University of Chinese Academy of Sciences
19A Yuquan Rd, Shijingshan District, Beijing 100049, P. R. China

P. Müller-Buschbaum
Heinz Maier-Leibnitz Zentrum (MLZ)
Technische Universität München
Lichtenbergstr. 1, 85748 Garching, Germany

X. Hu
Laboratory of Inorganic Synthesis and Catalysis
Institute of Chemical Sciences and Engineering
École Polytechnique Fédérale de Lausanne (EPFL)
ISIC-LSCI, BCH 3305, Lausanne 1015, Switzerland
E-mail: xile.hu@epfl.ch

 The ORCID identification number(s) for the author(s) of this article can be found under <https://doi.org/10.1002/adfm.202201675>.

© 2022 The Authors. Advanced Functional Materials published by Wiley-VCH GmbH. This is an open access article under the terms of the Creative Commons Attribution-NonCommercial License, which permits use, distribution and reproduction in any medium, provided the original work is properly cited and is not used for commercial purposes.

DOI: 10.1002/adfm.202201675

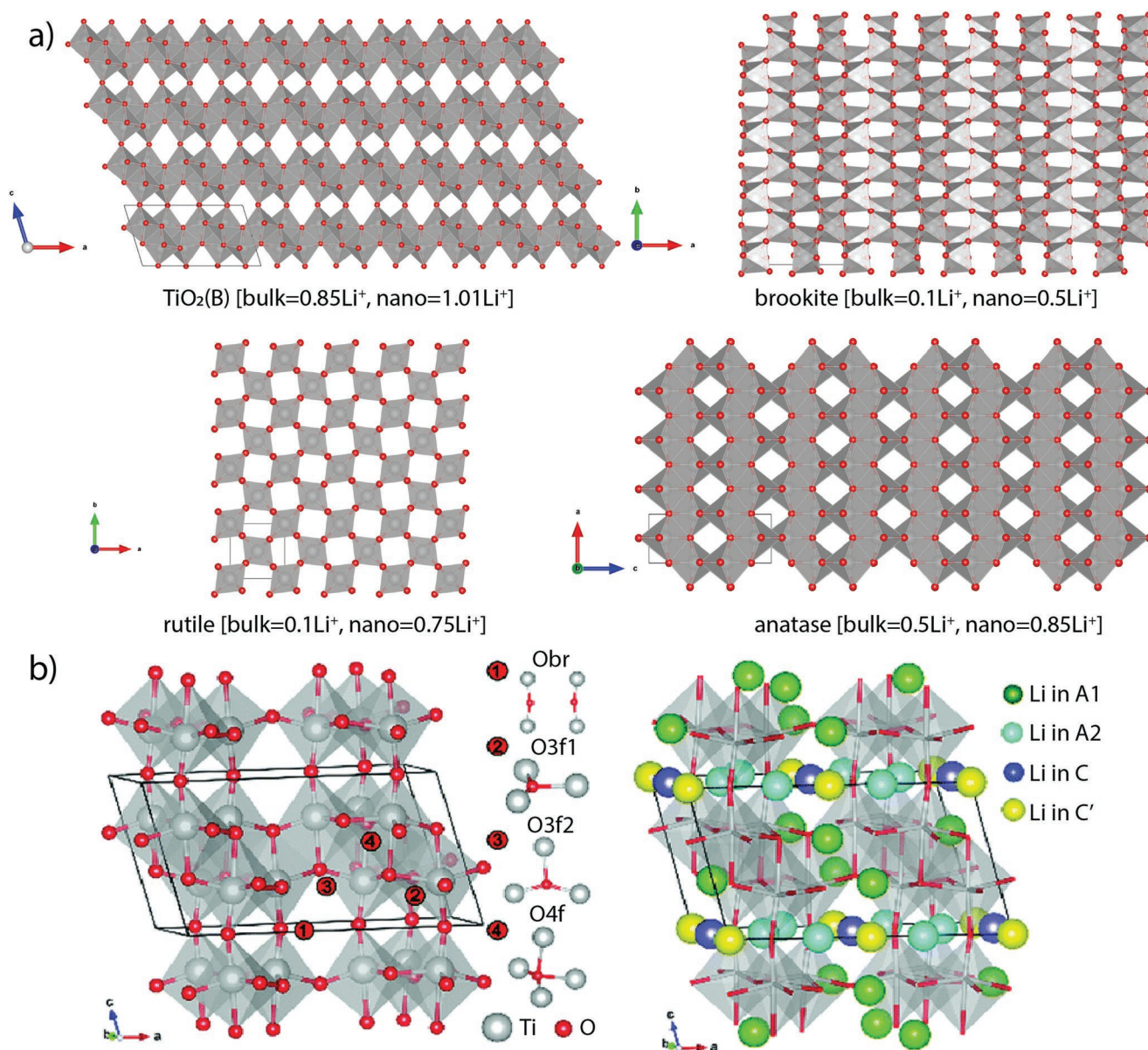


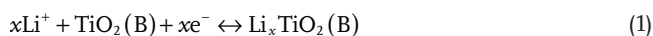
Figure 1. a) Crystal structures of the four TiO_2 polymorphs. Grey and red spheres represent O and Ti atoms. b) The detailed crystal structure of $\text{TiO}_2(\text{B})$ and available intercalation sites for Li atoms and spatial distribution. Reproduced with permission.^[16] Copyright 2019, Royal Society of Chemistry.

TiO_2 has four widely known polymorphs, anatase (tetragonal, space group: $I4_1/amd$), rutile (tetragonal, $P4_2/mnm$), brookite (orthorhombic, $Pbca$), and bronze ($\text{TiO}_2(\text{B})$) (monoclinic, $C2/m$), which all can react with lithium ions electrochemically and be applied as anodes for LIBs.^[8–10] The crystal structures of the four TiO_2 polymorphs and their corresponding Li-insertion abilities are shown in **Figure 1a**. Among the four polymorphs, $\text{TiO}_2(\text{B})$ has the highest theoretical capacity of 335 mAh g^{-1} and therefore naturally attracted considerable attention as a LIB anode in the last 20 years.^[11,12] Compared to the commercial graphite anode, $\text{TiO}_2(\text{B})$ can provide a comparable capacity but a higher discharge voltage plateau ($>1.7 \text{ V vs Li/Li}^+$), resulting in higher safety in operation.^[13] Moreover, in comparison with the high-capacity alloying-type anode materials that suffer from high-volume expansion during the cycling, $\text{TiO}_2(\text{B})$

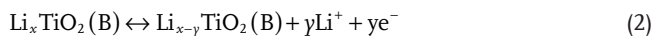
exhibits a much better structural stability and also allows for a faster lithium ion diffusion, which facilitates to achieve the fast-charging and long-lasting battery.^[14,15] Therefore, $\text{TiO}_2(\text{B})$ -based materials exhibit great competitiveness to act as the high-performance and safe anodes for LIBs. From a crystallography perspective, the crystalline structure of $\text{TiO}_2(\text{B})$ belongs to the monoclinic crystal system ($C2/m$). The unit cell consists of edge- and corner-sharing TiO_6 octahedra with an open channel paralleled to the b -axis and located between axial oxygen atoms. As shown in **Figure 1b**, there are four different intercalation sites for Li insertion in the $\text{TiO}_2(\text{B})$ crystal: the so-called A1, A2, C and C' sites.^[16,17] The A1 site locates in the center between the two O_{3f2} atoms in the TiO_6 octahedral layer and the A2 site occupies the position between the two O_{br} atoms in the O atomic layer. The C site locates in the center of the b -axis

channel cavity, while the C' site locates in a plane consisting of two O_{3f2} and O_{br} atoms. The lithiation/delithiation mechanism of $TiO_2(B)$ can be described by Equations (1) and (2).^[10,18]

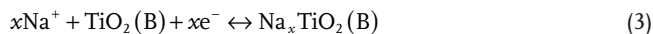
In the initial cycle:



In subsequent cycles:



Since the 2010s, sodium-ion batteries (SIBs) started to gain huge attention due to their great potential as the most promising substitute for LIBs in the future.^[19–20] Developing appropriate electrode materials is the key point to promote the real application of SIBs. Because of the unique open channel structure, $TiO_2(B)$ can also act as a good Na-insertion host, and the sodiation/desodiation processes are shown by Equation (3).^[11–21]



Although electrochemical performance and application potential of $TiO_2(B)$ anodes have been demonstrated by a number of studies, several critical drawbacks have significantly hampered their practical applications.^[13,22] First, even though the theoretical capacity of $TiO_2(B)$ is comparable to that of a graphite anode, it is not facile to fully realize the total capacity for actual applications due to limited electrochemical kinetics. Second, though bare $TiO_2(B)$ has demonstrated its relatively stable cycling stability, it still suffers from the gradual capacity decay during the long-term cycling process, which is a consequence of structural deterioration caused by volume change in repeated lithium-ion insertion/extraction processes. Thirdly, rate capability at high current densities is limited due to its poor lithium ionic and electronic conductivity. To tackle these issues, extensive theoretical and experimental studies have been performed in the last few decades covering the fundamental electrochemical mechanism investigation and synthesis of new materials with controlled crystallinity, morphology, bulk composition, and lattice modification.^[23–25] The crystallinity significantly influences the lithium-ion intercalation mechanism. The morphology, such as the size and shape of the $TiO_2(B)$, plays an important role in the electrochemical kinetics of the lithium-ion insertion/extraction processes. Bulk composition and lattice modification of TiO_2 provide a promising route to overcome the drawbacks of TiO_2 by enhancing the electrochemical kinetics and suppressing undesirable side effects.

Constructing nanostructured $TiO_2(B)$ materials and corresponding composites has become the mainstream strategy to improve the electrochemical performance of $TiO_2(B)$ -based anodes. Various $TiO_2(B)$ nanostructures have been developed and applied as anodes for LIBs and SIBs, including nanowires/nanofibers, nanotubes, nanorods/nanobelt, nanosheet, nanoparticles, and hierarchical spheres. The structure and morphology of $TiO_2(B)$ anode materials play key roles in their final electrochemical performance. Therefore, we will briefly discuss the formation mechanisms and representative synthesis methods of these $TiO_2(B)$ nanostructures. $TiO_2(B)$ nanowires can be fabricated by a hydrothermal reaction between NaOH

and anatase TiO_2 , followed by acid washing and calcination.^[26] Generally, the reaction between anatase TiO_2 and NaOH can produce layered sodium hydrogen titanate. With ongoing the hydrothermal reaction, the formed layered sodium hydrogen titanate gradually grows, splits, and wraps into cylindrical structure.^[27] The driving force for curving layered structures into cylindrical structure was believed to be the mechanical stress due to the non-uniform growth and imbalance of the multi-layered structures, resulting in the wrapping tendency of layers to decrease the surface energy.^[28] The following acid washing can convert the sodium hydrogen titanate into the hydrogen titanate via ion exchange.^[26,29] After final calcination, the $TiO_2(B)$ nanowires are obtained. $TiO_2(B)$ nanotubes can be synthesized by a similar hydrothermal approach with a lower reaction temperature and less volume of NaOH solution.^[28,30] Moreover, $TiO_2(B)$ nanorods/nanobelts can also be prepared by a similar hydrothermal method with different reaction conditions.^[31–32] It should be noted that such hydrothermal reaction between anatase TiO_2 and NaOH is highly sensitive to the reaction conditions, such as the reaction temperature, the amount of reactant, and the reaction duration. Small changes in reaction conditions can lead to obvious differences in the structure and morphology of the final products.^[33] Regarding $TiO_2(B)$ nanosheets, they can be synthesized by a one-step hydrolysis reaction of $TiCl_3$ in ethylene glycol.^[34] Generally, $TiO_2(B)$ nanoparticles can be prepared by a multi-step method that involves precursor preparation (alkali titanates), H^+ ion-exchange reaction, and final calcination for dehydration.^[35–36] This procedure is also similar to that of 1D $TiO_2(B)$ nanomaterials. After improvements, $TiO_2(B)$ nanoparticles can be synthesized from a water-soluble titanium complex via a one-step hydrothermal process.^[35,37] In recent years, with the development of synthesis techniques for nanomaterials, more and more $TiO_2(B)$ -based anodes with hierarchical and hollow nanostructures have been successfully fabricated.^[38–41] By applying self-assembly and template-induced approaches, these delicate and high-performance $TiO_2(B)$ -based anodes can be achieved.

Studies on the $TiO_2(B)$ anode have evolved significantly over the last few decades. However, to our best knowledge, a systematic review with a chronicle perspective on the $TiO_2(B)$ anode is not existing so far.^[19,24–25,42–45] In this review, the evolution of the studies on the $TiO_2(B)$ anode in the last few decades is addressed comprehensively. Through this review, it is possible to draw a whole picture of the basic research activities on the $TiO_2(B)$ anodes for both LIBs and SIBs. To elaborate this topic in a better way, this review is divided into several parts based on different classifications. First, the time from the 1980s to the present is divided into several time frames according to the status of the research work performed in the specified time range. Second, the research activities in a specific time frame are generally grouped based on the morphologies of the $TiO_2(B)$. Both the theoretical investigations and experimental studies are addressed for $TiO_2(B)$.

2. Early Stage of $TiO_2(B)$ Anodes: Before 2000

The bronze phase TiO_2 , $TiO_2(B)$, was reported by R. Marchand and M. Tournoux in 1980.^[46] $K_2Ti_4O_9$ was first hydrolyzed in a nitric acid solution to form $H_2Ti_4O_9 \cdot H_2O$, which was completely

dehydrated at 500 °C to produce TiO₂(B).^[46,47] The powder X-ray diffraction (XRD) pattern indicated a monoclinic unit cell with the lattice parameters of $a = 12.163(5)$ Å, $b = 3.735(2)$ Å, $c = 6.513(2)$ Å, $\beta = 107.29(5)^\circ$. The TiO₂(B) structure belonged to the ReO₃ type, where the smallest block of the ReO₃ structure contained four ReO₃ chains. The 3D framework of the TiO₂(B) was constructed by edge-sharing subunits. The packing of TiO₂(B) could be defined as CCP of oxygen where 1/8 of the oxygen atoms were missing.^[48] Besides XRD, high-resolution electron micrographs were acquired and interpreted to determine the positions of the titanium cations within the unit cell.^[49]

It was found difficult to stabilize the TiO₂(B) modification without a certain content of K₂Ti₈O₇, where the potassium-free sample was ready to be converted to anatase during the dehydration process at 500 °C.^[48] A slow phase conversion from bronze to anatase was observed by XRD between 600 and 700 °C.^[46] To resolve this issue, new approaches were developed to synthesize TiO₂(B) with enhanced structure stability, where heat treatment was performed at a relatively low temperature.^[50,51] T. P. Feist and P. K. Davies reported a soft chemical synthesis of TiO₂(B) from a layered titanate.^[51] A titanate of alkaline metal (A₂Ti_nO_{2n+1}, A = Na, K, Cs; 3 ≤ n ≤ 6) was subjected to proton exchange, followed by a dehydration process below 350 °C. As a result, the protonated titanate H₂Ti₃O₇ compound underwent a series of structure re-organization during the dehydration process, including condensation of the layered structure, nucleation, and growth of the TiO₂(B)-like the intermediate and final formation of the TiO₂(B).

The studies on the lithiation behavior of the TiO₂(B) were initiated since the discovery of the TiO₂(B) modification.^[48] R. Marchand et al. pointed out that it was possible for the TiO₂(B) to take 0.85 Li through either chemical reaction with BuLi or electrochemical lithiation.^[46] B. Zachau-Christiansen et al. analyzed the structure of the lithiated TiO₂(B).^[48] The results indicated that the TiO₂(B) phase possessed open structures, which enabled it an excellent host for lithium ion intercalation. The free radius of the channels was ≈0.58 Å, which was comparable to the free radius of the lithium ion (0.68 Å). The nuclear magnetic resonance (NMR) investigations suggested that the lithium ions tended to occupy the square pyramidal site at the top and bottom of the open channel. The TiO₂(B) can host a maximal Li uptake of 0.5 Li/Ti in combination with a liquid electrolyte at 25 °C (Li/LiAsF₆, PC) and with a polymer electrolyte at 120 °C (LiCF₃SO₃/PEO). The differential capacity profiles exhibited narrow peaks indicating weak attractive forces between the inserted lithium ions, which were not strong enough to promote two-phase separation during the lithiation process. Ordered structures showed a ratio Li/Ti of 0.33 and 0.5 at room temperature and 0.13 of Li/Ti at 120 °C. The Li/Ti of 0.5 indicated that one crystallographic site was occupied, where the Li/Ti of 0.125 suggested that one lithium ion inserted into each unit cell. The results showed that the lithium uptake was lower compared to the previously reported work.

In a short summary, the discovery of TiO₂(B) opened a new gate for the studies of Ti-based materials and LIB anodes. During this stage, the related studies mainly focused on the synthesis methods of TiO₂(B) and the exploration of its lithiation/delithiation mechanism as the anode for LIB.

3. Emerging Stage of TiO₂(B) Anodes: 2000–2009

Following the preliminary studies in the 1980s and 1990s, TiO₂(B) had started to attract increasing attention since 2000. Nanomaterial science significantly advanced the progress of the studies on the TiO₂(B) anodes. In 2004, A. R. Armstrong et al. reported a facile synthesis of TiO₂(B) nanowires via a hydrothermal treatment of anatase TiO₂ in 15 M NaOH solution at 170 °C, followed by acid washing and heating at 400 °C in air.^[26] Following this routine, the layered titanate was successfully converted to nanowires with typical diameters of 20–40 nm and lengths of 2–10 μm (Figure 2a). The relatively low annealing temperature suppressed phase transformation of the TiO₂(B) into other modifications of TiO₂. The authors proved that the TiO₂(B) nanowires could achieve lithium uptake of Li_{0.82}TiO₂, corresponding to a discharge capacity of 275 mAh g⁻¹ due to enhanced electronic and ionic conductivity. Further electrochemical performance investigation by the same group indicated that the lithium uptake could reach Li_{0.91}TiO₂ corresponding to 305 mAh g⁻¹, which was much higher than those of the Li₄Ti₅O₁₂ and TiO₂ anatase phase.^[29,52] A small irreversible capacity loss at the first cycle was observed, which was confirmed not due to the formation of the solid electrolyte interface (SEI) layer. The TiO₂(B) nanowire anode presented good capacity retention with <0.1% capacity decay per cycle at 50 mA g⁻¹. The same group further investigated the lithium intercalation mechanism of the TiO₂(B) nanowires. It was found that the TiO₂(B) nanowires exhibited a superior rate performance compared to the anatase TiO₂ nanoparticles and bulk TiO₂(B).^[52] The TiO₂(B) nanowires could accommodate both lithium ion and electrons, which made it both ionic and electronic conductive. The high reversible capacity, superior rate performance, and appropriate lithiation potential made the TiO₂(B) nanowires a promising LIB anode. Based on the above work, the authors further evaluated the electrochemical performance of the TiO₂(B) nanowire anode in a full cell configuration, where gel electrolyte and cathode of LiFePO₄ or LiNi_{0.5}Mn_{1.5}O₄ were used.^[53] The average potential of the as-prepared full cell could reach ≈2–3 V. The results showed that the full cell exhibited good cyclic stability and rate performance, where 80% of the low-rate capacity was maintained at 5 C. S. Pavasupree et al. synthesized TiO₂(B) nanofibers by calcining the as-synthesized titanate nanofibers at 400 °C for 4 h in the air, which was prepared by hydrothermal treatment of natural rutile sand.^[54] The TiO₂(B) nanofibers had diameters of from 20 to 100 nm and lengths of from 10 to 100 μm. M. Zukalova et al. synthesized phase pure TiO₂(B) microfibers starting from amorphous TiO₂, which reacted with Cs₂CO₃ through a solid-state reaction, followed by ion exchange and calcination in air.^[55] The cyclic voltammetry measurement indicated that the lithium insertion into the TiO₂(B) microfibers was dominated by a pseudocapacitive faradaic process. This unique process was associated with the parallel channels perpendicular to the (010) facet of the TiO₂(B) nanocrystals, which were freely accessible for the lithium ion diffusion.

M. Wilkening et al. used ⁷Li spin-alignment echo nuclear magnetic resonance (SAE NMR) to investigate the lithium diffusion behavior of the lithiated TiO₂(B) nanowires of Li_xTiO₂ (0 < x ≤ 0.9).^[56] The lithium ion self-diffusion in the nanowires

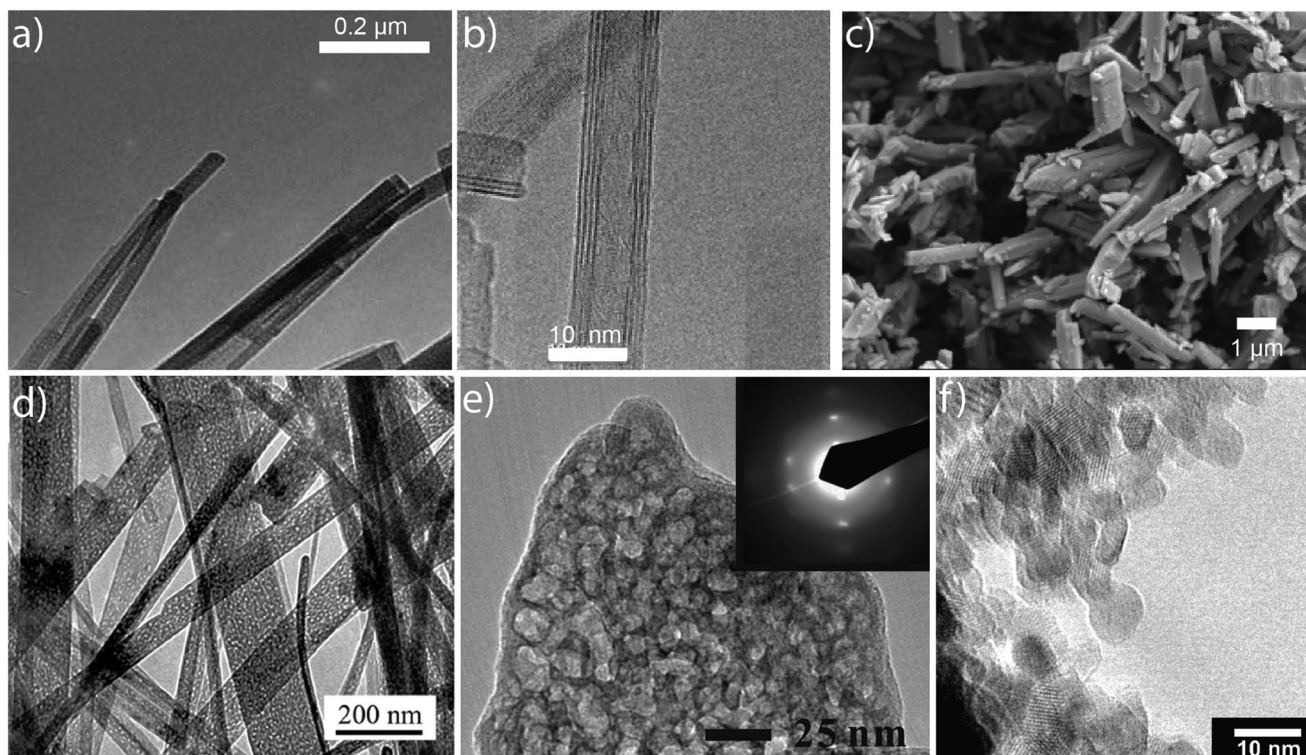


Figure 2. a) Transmission electron microscopy (TEM) image of the $\text{TiO}_2(\text{B})$ nanowires. Reproduced with permission.^[26] Copyright 2004, Wiley-VCH. b) TEM image of the $\text{TiO}_2(\text{B})$ nanotubes. Reproduced with permission.^[30] Copyright 2005, Royal Society of Chemistry. c) Scanning electron microscopy (SEM) image of the $\text{TiO}_2(\text{B})$ nanorods. Reproduced with permission.^[60] Copyright 2008, Elsevier B.V. d) TEM image of the $\text{TiO}_2(\text{B})$ nanoribbons. Reproduced with permission.^[61] Copyright 2008, American Chemical Society. e) TEM image of the porous $\text{TiO}_2(\text{B})$ nanosheet. Reproduced with permission.^[62] Copyright 2009, American Chemical Society. f) TEM image of the $\text{TiO}_2(\text{B})$ nanoparticles. Reproduced with permission.^[63] Copyright 2007, American Chemical Society.

of the $\text{Li}_{0.3}\text{TiO}_2$ was found to be highly heterogeneous. The decay rates determined by the ^7Li SAE NMR suggested that the overall lithium hopping rate was quite slow. Considering that the $\text{TiO}_2(\text{B})$ nanowires exhibited a good rate performance, it was reasonable to conclude that the shortened electron and lithium ion diffusion lengths in the nanowires compensated for the slow hopping rate. M. Wilkening et al. also used simulated echo NMR to characterize the dynamic properties of the lithium intercalated $\text{TiO}_2(\text{B})$ nanowires.^[57] It was found that the lithium self-diffusion was very slow, with an activation energy of 0.48 eV. G. Armstrong et al. reported the first synthesis of $\text{TiO}_2(\text{B})$ nanotubes through a hydrothermal reaction of the anatase TiO_2 powder in an aqueous NaOH solution.^[30] The outer tube diameter was in the range from 10 to 20 nm, as shown in Figure 2b. The $\text{TiO}_2(\text{B})$ nanotube exhibited a lithiation capacity of $\text{Li}_{0.98}\text{TiO}_2$, which was higher than the TiO_2 nanowires ($\text{Li}_{0.91}\text{TiO}_2$). The same group further evaluated the electrochemical performance details of the $\text{TiO}_2(\text{B})$ nanotubes as the LIB anodes.^[58] It was found that the $\text{TiO}_2(\text{B})$ displayed a capacity of 338 mAh g^{-1} with a composition of $\text{Li}_{1.01}\text{TiO}_2$ at a potential of around 1.5 V versus Li/Li^+ . A good rate performance was also observed with a capacity of 95 mAh g^{-1} at 2 A g^{-1} . An average capacity-decay rate of 0.16% per cycle was observed. The initial Coulombic efficiency of around 71% was achieved, where the Coulombic efficiencies in the following cycles were almost 100%. E. Morgado Jr et al. studied the phase transformation behavior of the hydrogen titanate nanotubes to

achieve a controllable synthesis of the $\text{TiO}_2(\text{B})$ nanotubes.^[59] It was found that the $\text{TiO}_2(\text{B})$ nanotube was formed by heating the $\text{H}_2\text{Ti}_3\text{O}_7$ prepared with the hydrothermal reaction and subsequent ion-exchange treatment. A multi-step phase transformation was observed where the nanotubular structure was well retained. The phase transformation occurred between 120 and $400 \text{ }^\circ\text{C}$ through a topotactic mechanism with the formation of the intermediate nanostructured $\text{H}_2\text{Ti}_6\text{O}_{13}$ and $\text{H}_2\text{Ti}_{12}\text{O}_{25}$. It was recognized that the $\text{H}_2\text{Ti}_{12}\text{O}_{25}$ was the final layered intermediate phase, from which the $\text{TiO}_2(\text{B})$ nanotubes were formed.

M. Inaba et al. synthesized $\text{TiO}_2(\text{B})$ nanorods by protonating $\text{K}_2\text{Ti}_4\text{O}_9$ (Figure 2c), followed by dehydration treatment.^[60] The $\text{TiO}_2(\text{B})$ nanorods delivered a discharge capacity of from 200 to 250 mAh g^{-1} at about 1.6 V versus Li/Li^+ . The capacities were comparable to those of the $\text{TiO}_2(\text{B})$ nanowires and nanotubes. Good cyclic stability was achieved with a discharge capacity of 170 mAh g^{-1} after 650 cycles. The $\text{TiO}_2(\text{B})$ nanorods also exhibited high rate capability, which reached 106 mAh g^{-1} at 10 C. In this work, the applicability of various electrolyte systems for the $\text{TiO}_2(\text{B})$ anodes was also investigated. The $\text{TiO}_2(\text{B})$ anodes could present good charge and discharge characteristics in most ethylene carbonate-based electrolyte systems. However, some electrolytes, such as lithium tetrafluoroborate (LiBF_4), propylene carbonate, and gamma-butyrolactone solutions, were not compatible with the $\text{TiO}_2(\text{B})$ anodes. The poor compatibility could be attributed to solvent decomposition and excessive surface film formation in these electrolyte solutions.

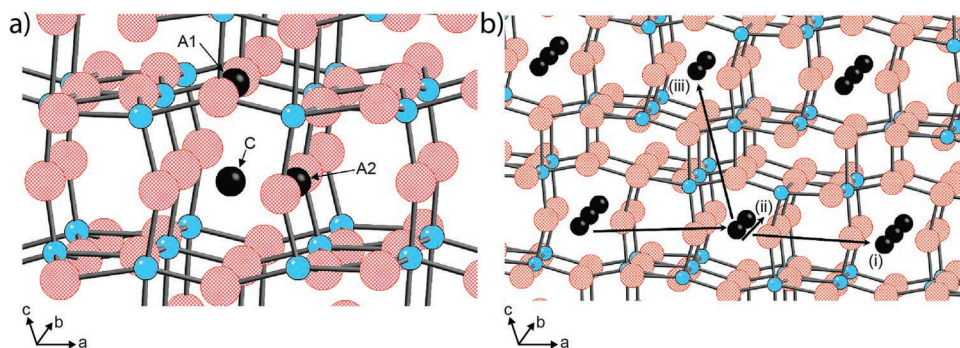


Figure 3. a) Possible lithium intercalation sites labeled C, A1, and A2. b) Li ions diffusion paths (black arrows) between C sites. Oxygen atoms, Ti atoms, and Li ions are displayed by the red, blue, and black spheres, respectively. Reproduced with permission.^[65] Copyright 2009, American Chemical Society.

Q. Li et al. synthesized single crystal $\text{TiO}_2(\text{B})$ nanoribbons with high-density nanocavities through a hydrothermal reaction.^[61,64] The $\text{TiO}_2(\text{B})$ nanoribbons grew along the (010) direction with widths of from 30 to 200 nm and lengths of several micrometers, as displayed in Figure 2d. Due to the existence of a high density of the nanocavities, the specific surface area of the $\text{TiO}_2(\text{B})$ nanoribbons reached $305 \text{ m}^2 \text{ g}^{-1}$. The $\text{TiO}_2(\text{B})$ nanoribbons exhibited higher capacities than those of the $\text{TiO}_2(\text{B})$ nanowires and nanotubes. The high-density nanocavities were supposed to make a significant contribution to the electrochemical performance. M. C. Tsai et al. synthesized mesoporous $\text{TiO}_2(\text{B})$ nanosheets (Figure 2e) by thermal treatment of the formic acid terminated titanate nanosheets above $250 \text{ }^\circ\text{C}$, which was prepared with a sol-gel reaction between titanium tetraisopropoxide and formic acid.^[62] By tuning the calcination temperature, the relative content of the $\text{TiO}_2(\text{B})$ nanosheets could be changed. The initial discharging capacity of the $\text{TiO}_2(\text{B})$ nanosheets reached 357 mAh g^{-1} . However, the initial Coulombic efficiency and cyclic stability still needed to be improved. M. Kobayashi et al. developed a one-step hydrothermal synthesis of $\text{TiO}_2(\text{B})$ nanoparticles (Figure 2f) using a water-soluble titanium glycolate complex as the precursor in the presence of $0.59 \text{ M H}_2\text{SO}_4$.^[63] The sulfuric acid played an important role in the formation of the single phase of $\text{TiO}_2(\text{B})$.

C. Arrouvel et al. utilized density functional theory (DFT) to calculate the critical issues of the $\text{TiO}_2(\text{B})$ related to the lithium insertion sites and diffusion paths.^[65] The calculated electronic structures suggested that the most favorable lithium intercalation site with the lowest energy was located in the square planar site (the C site) with slightly off-center in the b -axis channel when the lithium concentration was low ($x < 0.125$ for Li_xTiO_2), as shown in Figure 3a. For the lithiated $\text{TiO}_2(\text{B})$ with an x value > 0.25 , the intercalated lithium was supposed to occupy additional positions of the C site. The calculated cell voltages were consistent with the electrochemical measurements. The lithium ion diffusion paths with low energies of around 0.3 eV were identified, which was along the b -axis channel in the (010) direction (Figure 3b). Low diffusion energy of around 0.5 eV was derived along the (001) direction. The results indicated that the $\text{TiO}_2(\text{B})$ possessed high lithium ion mobility, which was anisotropic within the lattice. D. Panduwina et al. performed first-principle calculations on the intercalation behavior of the $\text{TiO}_2(\text{B})$ based on a generalized gradient approximation within

density functional theory.^[66] The authors identified three symmetry unique sites preferred for the occupation of the lithium ions at low lithium concentrations. The most stable site was proposed within the inter-lamellar region between successive sheets of the TiO_6 , where the lithium-lithium interaction was absent, and the lithium ions could be bonded to the oxygen atoms connecting the sheets. The lithium ion diffusion paths between the calculated sites were also elucidated. It was found that the lithium ions tended to be located at a site near to the TiO_6 octahedral layers. The lowest activation energy of 27 kJ mol^{-1} was derived from the lithium ion diffusion along the open channel parallel to the b -axis. Consequently, the lithium ions had to be promoted from the thermodynamically favored sites to the channels where the lithium ions could diffuse fast. When the lithium ion concentration was increased within the $\text{TiO}_2(\text{B})$ lattice, the lithium ions had to occupy the least intrinsically stable sites near the octahedral layers, where the unfavorable cation–cation interaction was minimized. This process caused the voltage to drop because the lithium ion mobility was lowered.

In the first ten years of the 21st century, the studies about $\text{TiO}_2(\text{B})$ anodes gained much progress. Various nanostructured $\text{TiO}_2(\text{B})$ materials were synthesized, including nanowires, nanotubes, nanorods, nanoribbons, nanosheets, and nanoparticles, which led to a great improvement of the electrochemical performance of $\text{TiO}_2(\text{B})$ LIB anodes. In addition, more synthesis methods of $\text{TiO}_2(\text{B})$ materials were also developed compared with those in the stage before. Furthermore, assisted with advanced characteristic techniques, an in-depth understanding of the lithiation/delithiation mechanism of $\text{TiO}_2(\text{B})$ anodes was achieved in this timeframe. The synthetic methods and electrochemical performance of representative studies about $\text{TiO}_2(\text{B})$ LIB anodes from 1980 to 2009 are summarized in Table 1.

4. Explosive Stage of $\text{TiO}_2(\text{B})$ Anodes: 2010–2015

Studies on the synthesis and application of $\text{TiO}_2(\text{B})$ expanded significantly from 2010 to 2015.^[10,15] Nanostructured $\text{TiO}_2(\text{B})$ with various morphologies was reported, where the synthesis, electrochemical performance, and structure-property correlations were covered.^[67] It became one of the central topics for the $\text{TiO}_2(\text{B})$ based LIB anodes. Besides the synthesis of the

Table 1. Summary on representative studies about TiO₂(B) LIB anodes from 1980 to 2009 (ICE: initial Coulombic efficiency; *n*: the *n*th cycle; CD: current density).

Representative anode	Synthetic method	ICE	Charge capacity [mAh g ⁻¹] (<i>n</i> , CD/rate)	Rate capacity [mAh g ⁻¹] (CD/rate)	Remark	Ref.
Early stage: before 2000						
TiO ₂ (B)	hydrolysis of K ₂ Ti ₄ O ₉ and dehydration of H ₂ Ti ₄ O ₉ ·H ₂ O (high temperature)	\	\	\	the first synthesis of TiO ₂ (B)	[46]
TiO ₂ (B)	proton exchange and dehydration of layered titanates (low temperature)	\	\	\	development of TiO ₂ (B) synthesis at a relatively low temperature	[51]
TiO ₂ (B)	followed from Ref. [46]	\	\	\	the initial study about Li insertion of TiO ₂ (B)	[48]
Emerging stage: 2000–2009						
TiO ₂ (B) nanowires	hydrothermal reaction between NaOH and TiO ₂ anatase	\	275 (1, 10 mA g ⁻¹)	\	the first synthesis of TiO ₂ (B) nanowires	[26]
TiO ₂ (B) nanowires	followed from Ref. [26]	\	≈200 (100, 50 mA g ⁻¹)	85 (3 A g ⁻¹)	\	[52]
TiO ₂ (B) nanowires	followed from Ref. [26]	\	(a)≈200 (100, C/5) (b)≈200 (100, C/5)	(a) ≈80 (5C) (b)≈78 (5C)	full-cell studies with LiFePO ₄ cathode (a) and LiNi _{0.5} Mn _{1.5} O ₄ cathode (b)	[29]
TiO ₂ (B) nanowires	followed from Ref. [26]	\	\	\	Li diffusion studies by NMR	[56–57]
TiO ₂ (B) nanotubes	hydrothermal reaction between NaOH and TiO ₂ anatase	\	≈300 (1, 10 mA g ⁻¹)	\	the first synthesis of TiO ₂ (B) nanotubes	[30]
TiO ₂ (B) nanotubes	followed from Ref. [30]	≈75%	≈225 (50, 50 mA g ⁻¹)	95 (2 A g ⁻¹)	\	[58]
TiO ₂ (B) nanorods	followed from Ref. [51]	≈66%	170 (650, C/6)	106 (10C)	\	[60]
TiO ₂ (B) nanoribbons	hydrothermal process and post treatments	\	≈225 (19, 67 mA g ⁻¹)	\	stable long-term cycling performance	[61]
TiO ₂ (B) nanosheets	reaction between TTIP and formic acid	≈57%	≈130 (20, \)	\	porous nanosheet	[62]
TiO ₂ (B) nanoparticles	one-step hydrothermal process	\	\	\	the first synthesis of TiO ₂ (B) nanoparticles by one-step process	[63]
TiO ₂ (B)	\	\	\	\	DFT study of TiO ₂ (B) anode	[65]

bare TiO₂(B) nanostructures, composition with electron conductive components such as carbonaceous materials, metals, and electron conductive polymers were applied to improve the electron conductivity of the nanoscale TiO₂(B).^[24] Heteroatom doping and incorporation of oxygen vacancies by self-doping were used extensively to modify the electronic structure and improve the electrochemical performance.^[25] Incorporation of high-capacity materials such as metal oxides, alloying elements, and metal sulfides was also explored to increase the overall capacities of the TiO₂(B) based composite anodes.^[43] Besides the LIB anodes, the applications of the TiO₂(B) based composites started to be extended to the SIB anodes.^[19] The theoretical studies on the fundamental electrochemical mechanism of the nanoscale TiO₂(B) were continued, where both the thermodynamic and kinetic issues were addressed.^[68,69]

4.1. TiO₂(B) Nanowires

TiO₂(B) nanowires were synthesized through hydrothermal reaction in alkaline solutions, followed by protonation treatment and dehydration at high temperatures.^[70–75] During this period, carbon materials, such as graphene (G) and hard carbon started to be applied to enhance the Li⁺ transport and mechanical strength of TiO₂(B) nanowire anodes.^[76–78] In 2014, X. Li et al. fabricated graphene nanoscrolls encapsulated TiO₂(B)

nanowires through a self-scrolling and template-free process.^[78] As shown in **Figure 4a**, the suspension of graphene oxide (GO) and TiO₂ nanoparticles were first hydrothermally treated in alkali solution, in order to generate amorphous titanate intermediates which could attach to the GO nanosheets. With the ongoing hydrothermal process, GO nanosheets were reduced into graphene nanosheets which started to be scrolled up to encapsulate titanate nanowires inside due to the strong adhesion between graphene nanosheets and titanates. After ion exchanging and heat treatment, the hybrids of graphene nanoscrolls encapsulated TiO₂(B) nanowires were obtained. The as-prepared TiO₂(B)-G nanowires have diameters of ≈200 nm, where the thicknesses of outside G nanoscrolls were ranged from 10 to 30 nm. Compared to the bare TiO₂(B), this hybrid anode exhibited enhanced electrochemical performance. Particularly, the TiO₂(B)-G nanowires retained a reversible capacity of 153 mAh g⁻¹ after 300 cycles under a high rate of 10C (1C = 335 mA g⁻¹). In addition, metal oxides including tin dioxide were composited with the TiO₂(B) nanowires to increase the overall capacities of the composite, where the TiO₂(B) nanowires could help to buffer the mechanical stress generated by the lithiation of the tin dioxide and tin to improve the cyclic stability.^[79–82]

Besides experimental studies on morphology control and composition, theoretical research was carried out to understand the fundamental electrochemical mechanism of the TiO₂(B)

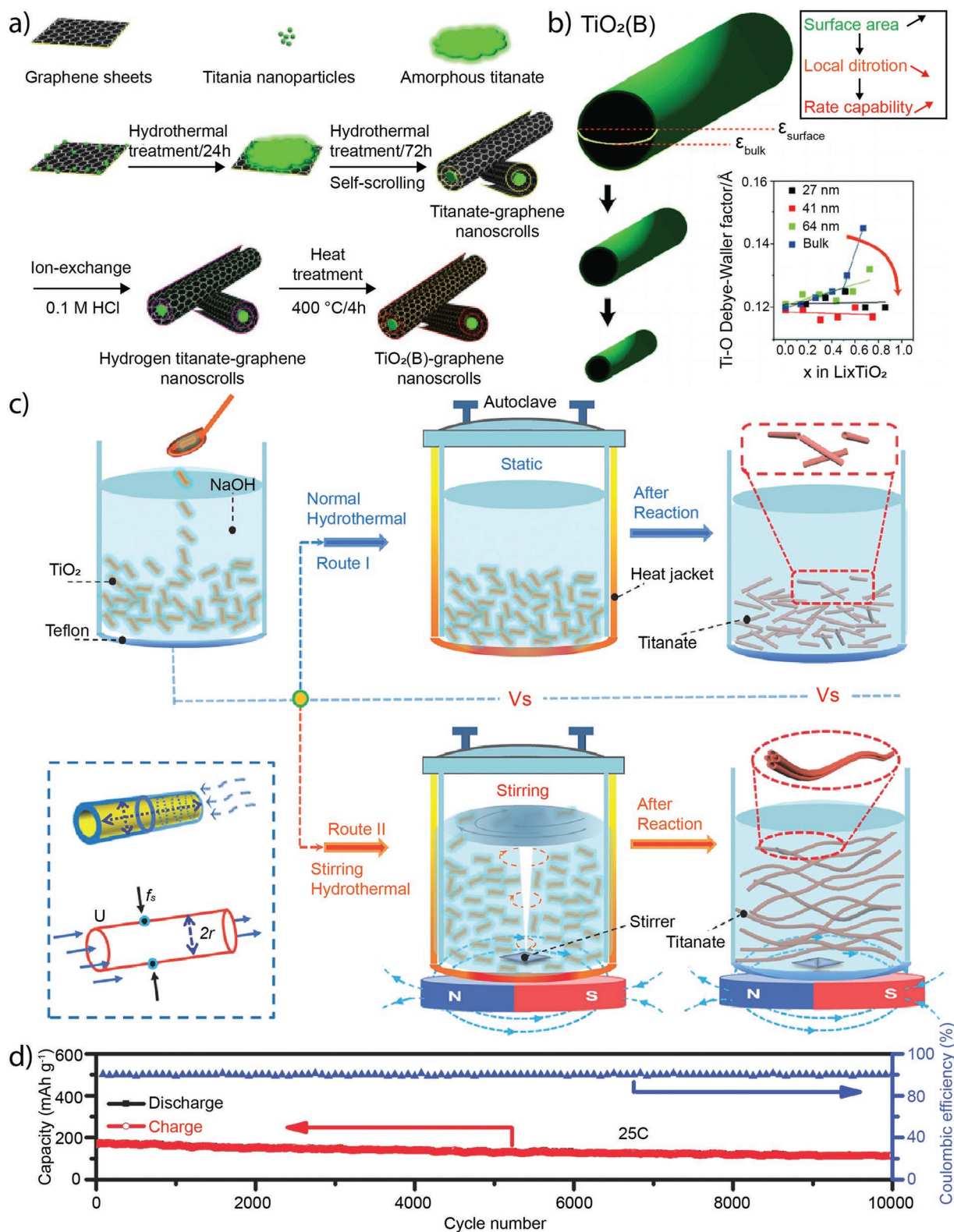


Figure 4. a) Schematic illustration of TiO₂(B)-graphene nanoscrolls synthesis process. Reproduced with permission.^[78] Copyright 2014, Elsevier B.V. b) Explanation of the nanosized effect on electronic/local structures and specific lithium-ion insertion property in TiO₂(B) nanowires. Reproduced with permission.^[18] Copyright 2011, American Chemical Society. c) Schematic illustration of the formation process of short and elongated nanotubular structures under normal and stirring hydrothermal processes; d) long-term cycling performance of elongated bending TiO₂(B) nanotube anode in LIB. Reproduced with permission.^[86] Copyright 2014, Wiley-VCH.

(B) nanowires. A. R. Armstrong et al. investigated structure evolution during the lithiation process of the $\text{TiO}_2(\text{B})$ nanowires by combining the powder neutron diffraction and DFT calculations.^[83] The authors identified three lithiated phases, $\text{Li}_{0.25}\text{TiO}_2(\text{B})$, $\text{Li}_{0.5}\text{TiO}_2(\text{B})$, and $\text{Li}_{0.9}\text{TiO}_2(\text{B})$. With the lithium content not >0.25 , the lithium was preferred to be inserted into the square planar site at the center of the b axis channel, which was the C site. When the lithium ratio was further increased to the level between 0.25 and 0.5, it was found that the A1 site was more favorable for intercalation than the C site. With the lithium concentration lifted to the highest level, the results suggested that both the A1 site and A2 site were inserted equally, both of which exhibited a five-coordination pattern. Furthermore, the authors also found that the volume of the unit cell was increased along with increasing lithium concentration. An anisotropic shape change with the unit cell was also observed, where the unit cell was extended along the b direction significantly. The voltage change calculated based on the DFT was found consistent with the experimental results, where the different potential regions were correlated with the lithium insertion into different sites in the lattice. Finally, the authors pointed out that the bulk $\text{TiO}_2(\text{B})$ phase exhibited a similar lithiation mechanism to the $\text{TiO}_2(\text{B})$ nanowires. M. V. Koudriachova et al. elucidated the mechanism responsible for the enhanced lithiation performance with the $\text{TiO}_2(\text{B})$ nanowires using ab initio calculations.^[84] The calculations indicated that the $\text{TiO}_2(\text{B})$ nanowires exhibited a capacitive behavior with the lithiation x value not >0.5 , where the high surface area and rich insertion sites of the $\text{TiO}_2(\text{B})$ nanowires were crucial for this process.^[85] The surface intercalated lithium ions were independently transported into the interior region of the $\text{TiO}_2(\text{B})$ nanowires in a radial style. With the lithium concentration increased to the x value >0.5 , it was found that the lithium intercalation process was diffusion-limited, which was enhanced due to the nanoscale structure feature. Nevertheless, the author pointed out that the diffusion mechanism could not be fully fulfilled, which resulted in obstacle to access the lithium storage site. Consequently, it was unable to reach the full theoretical capacity of the $\text{TiO}_2(\text{B})$ nanowires.

T. Okumura et al. synthesized $\text{TiO}_2(\text{B})$ nanowires with different sizes and investigated the nano-size effect on the lithium ion intercalation properties using X-ray absorption spectroscopy (XAS) and X-ray absorption near-edge structure analysis (XANES).^[18] It was found that the discharge capacities below 1.45 V of all the $\text{TiO}_2(\text{B})$ nanowires with different sizes did not vary with the applied current densities. However, the discharge capacities exhibited above 1.45 V decreased with increasing current densities. It was therefore proposed that the lithium intercalation process below 1.45 V was associated with the surface region in the space charge layer. The results indicated that the local and electronic structures of the surface of the $\text{TiO}_2(\text{B})$ nanowires were different from those of the bulk phase of the $\text{TiO}_2(\text{B})$ nanowires. Furthermore, the authors also found that the band energy of the $\text{TiO}_2(\text{B})$ nanowire surface was lower compared to that of the bulk counterpart. The space charge layer of the $\text{TiO}_2(\text{B})$ nanowires possessed different structures from that of the bulk $\text{TiO}_2(\text{B})$, as indicated by both the XAS data and discharge profiles. It was suggested by the authors that the lithium intercalation into the $\text{TiO}_2(\text{B})$ nanowires were smooth

because of the well-maintained structure of the space charge layer during the lithium insertion process. Therefore, it was possible to enhance the rate capability of the $\text{TiO}_2(\text{B})$ nanowires by increasing the space charge layer region on the $\text{TiO}_2(\text{B})$ nanowires. The results from the authors are summarized vividly in Figure 4b.

In summary, the theoretical investigations identified three lithiated phases of $\text{Li}_{0.25}\text{TiO}_2$, $\text{Li}_{0.5}\text{TiO}_2$, and $\text{Li}_{0.9}\text{TiO}_2$, where the lithium ions were inserted into different positions in the $\text{TiO}_2(\text{B})$ lattice. It was revealed that the capacity of the $\text{TiO}_2(\text{B})$ nanowires originated from the combination of capacitive (Li_xTiO_2 with $x < 0.5$) and diffusion process (Li_xTiO_2 with $x > 0.5$). Correspondingly, the discharge capacity with the voltage above 1.45 V was ascribed to the bulk lithiation mechanism, while the capacity below 1.45 V belonged to the surface storage process. The existence of the space charge layer during the lithiation process was proposed, which was beneficial for maintaining high rate capability. Electrochemical performance improvement could be achieved based on the fundamental understanding of the electrochemical mechanism of the $\text{TiO}_2(\text{B})$ nanowires.

4.2. $\text{TiO}_2(\text{B})$ Nanotubes

$\text{TiO}_2(\text{B})$ nanotubes were synthesized through hydrothermal reaction in alkaline solutions using anatase TiO_2 powder as the starting material, where experimental details were systematically modified to tune the respective morphology.^[11,86–88] Compositing with $\text{TiO}_2(\text{B})$ nanotubes was explored including carbon, metal, and metal oxides.^[89–91] Introducing doping atoms into the $\text{TiO}_2(\text{B})$ lattice was reported.^[92] All of these strategies tended to enhance further the electrochemical performance of the $\text{TiO}_2(\text{B})$ nanotubes. Y. Tang et al. developed a stirring hydrothermal method to synthesize elongated bending $\text{TiO}_2(\text{B})$ nanotubes (Figure 4c).^[86] TiO_2 nanoparticles were first dispersed in NaOH aqueous solution. With the normal hydrothermal process (the route I), the short $\text{TiO}_2(\text{B})$ nanotubes (several-hundred nanometers) were obtained, which could be attributed to the slow dissolution-recrystallization process and low growth kinetic of nanotube at the static condition. When added magnetic stirring during the hydrothermal process, the length of $\text{TiO}_2(\text{B})$ nanotubes could be elongated significantly to the micrometer scale. As explained by the authors, the mechanical force of stirring during the synthetic process had four important effects, including breaking the dissolution-recrystallization equilibrium, improving the mass transport, forming the bending nanotubes, and preventing the sedimentation. In terms of electrochemical performance, the elongated bending $\text{TiO}_2(\text{B})$ nanotubes gained exceptional cyclic stability, and rate performance due to the cross-linking architecture originating from the bending structure feature. In particular, this $\text{TiO}_2(\text{B})$ anode retained a reversible capacity of 114 mAh g^{-1} after 10 000 cycles at a high current density of 25 C ($1 \text{ C} = 335 \text{ mA g}^{-1}$), as shown in Figure 4d.

Besides, S. Brutti et al. proved that the dominant source of the initial irreversible capacity of the $\text{TiO}_2(\text{B})$ nanotube originated from the reaction between the $\text{TiO}_2(\text{B})$ nanotube surface and the electrolyte, not from the lithiation process within

the nanotube.^[87] Based on this finding, the authors treated the TiO₂(B) nanotube with lithium ethoxide, where the initial coulombic efficiency was increased from 74% to 93% with a capacity of 237 mAh g⁻¹ at 0.05 C (1 C = 335 mA g⁻¹). The surface treatment generated Li₂CO₃ on the nanotube surface, which helped to stabilize the interface during the lithiation/delithiation process. Compared to the surface-treated TiO₂(B) nanotube, the pristine TiO₂(B) nanotube possessed ROCO₂Li and P-O-C functional groups on the surface as a result of the hydrolysis of LiPF₆. Good rate performance was demonstrated by the surface-treated TiO₂(B) nanotubes with a reversible capacity of 134 mAh g⁻¹ at 5 C.

4.3. TiO₂(B) Nanorods

Compared to the TiO₂(B) nanowires and nanotubes, only a few studies were reported about the TiO₂(B) nanorods. Solid-state reaction, the hydrothermal reaction in either alkaline or acid solution was employed to synthesize the TiO₂(B) nanorods.^[32,93] In 2013, V. Aravindan et al. fabricated TiO₂(B) nanorods by a conventional hydrothermal approach.^[32] In the half-cell test, the Li//TiO₂(B) cell maintained a reversible capacity of about 130 mAh g⁻¹ up to 500 cycles at a current density of 150 mA g⁻¹. In the full-cell test, accompanied by the electrospinning PVDF-HFP (polyvinylidene fluoride-co-hexafluoropropylene) membrane as the separator, the LiMn₂O₄//TiO₂(B) cell exhibited a stable cyclability, which retained a capacity retention of about 67%. Moreover, the full cell also could reach a reversible capacity of ≈60 mAh g⁻¹ at a high current density of 2 A g⁻¹. Compositing the TiO₂(B) nanorods with other TiO₂ polymorphs such as anatase were also reported, where the effect of the

anatase phase on the electrochemical performance was investigated.^[94,95]

Regarding the fundamental study, Y. Ishii et al. investigated the lithium insertion mechanism of a rod-like single-phase TiO₂(B) electrode by in situ synchrotron XRD technique.^[96] The single-phase TiO₂(B) anode material was prepared according to a multi-step method reported by R. Marchand et al.,^[46] and then the as-obtained single-phase TiO₂(B) material was applied to assemble a custom-made cell for the in situ XRD measurement, as illustrated by Figure 5a,b. The custom-made two-electrode type cell was equipped with two crystalline diamond windows to ensure the high transmittance for X-rays. As shown in Figure 5c, the position shifts of the diffraction peaks indicated the reversible structural changes of the TiO₂(B) electrode during the charging and discharging process. Specifically, the peaks gradually shifted toward smaller-angle regions during the discharging process (lithium insertion) and inversely toward larger-angle regions in the charging process (lithium extraction). In the lithiation process (1.85–1.30 V vs Li/Li⁺), the number of diffraction peaks and the corresponding relative intensities almost remained constant, indicating that TiO₂(B) could accommodate lithium ions with maintaining its initial monoclinic crystal structure. With Rietveld refinement of the in situ XRD data at 1.3 V versus Li/Li⁺, the structure of TiO₂(B) in the fully lithiated state was confirmed as Li_{0.8}TiO₂(B). Besides, based on the analysis of extracted crystal lattice parameters (*a*, *b*, *c*, β) from the diffraction peaks, the results indicated that the length of the *a*-axis and *b*-axis gradually increased while the length of the *c*-axis and angle-β almost remained constant during the lithium insertion process. In addition, by focusing on the evolution of the (020) peak, as shown in Figure 5d, the changes of the decomposed peak intensities indicated a typical

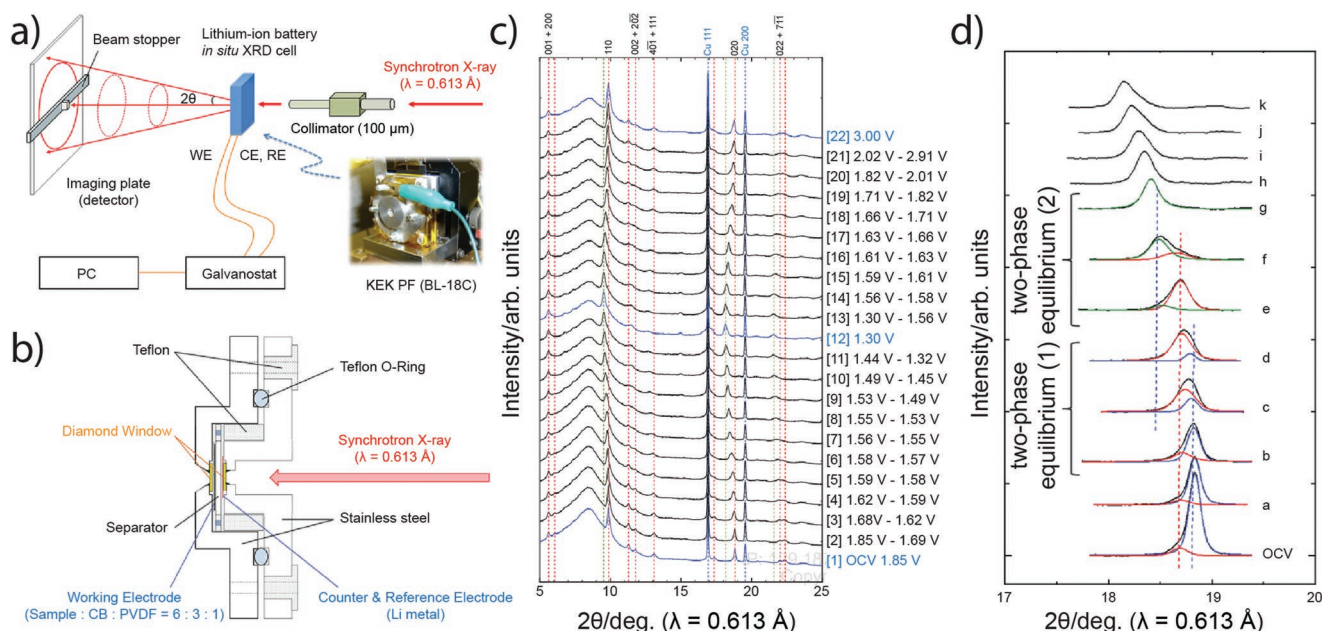


Figure 5. Schematic figures of a) the beam line configuration for the in situ XRD measurement and b) the structure of in situ XRD cell. c) In situ XRD patterns of the single-phase TiO₂(B) electrode obtained with continuous galvanostatic charging/discharging cycles at 30 mA g⁻¹. d) Zoom-in in situ XRD patterns of the (020) peak collected with continuous galvanostatic charging/discharging cycles at 25 mA g⁻¹. Reproduced with permission.^[96] Copyright 2012, American Scientific Publishers.

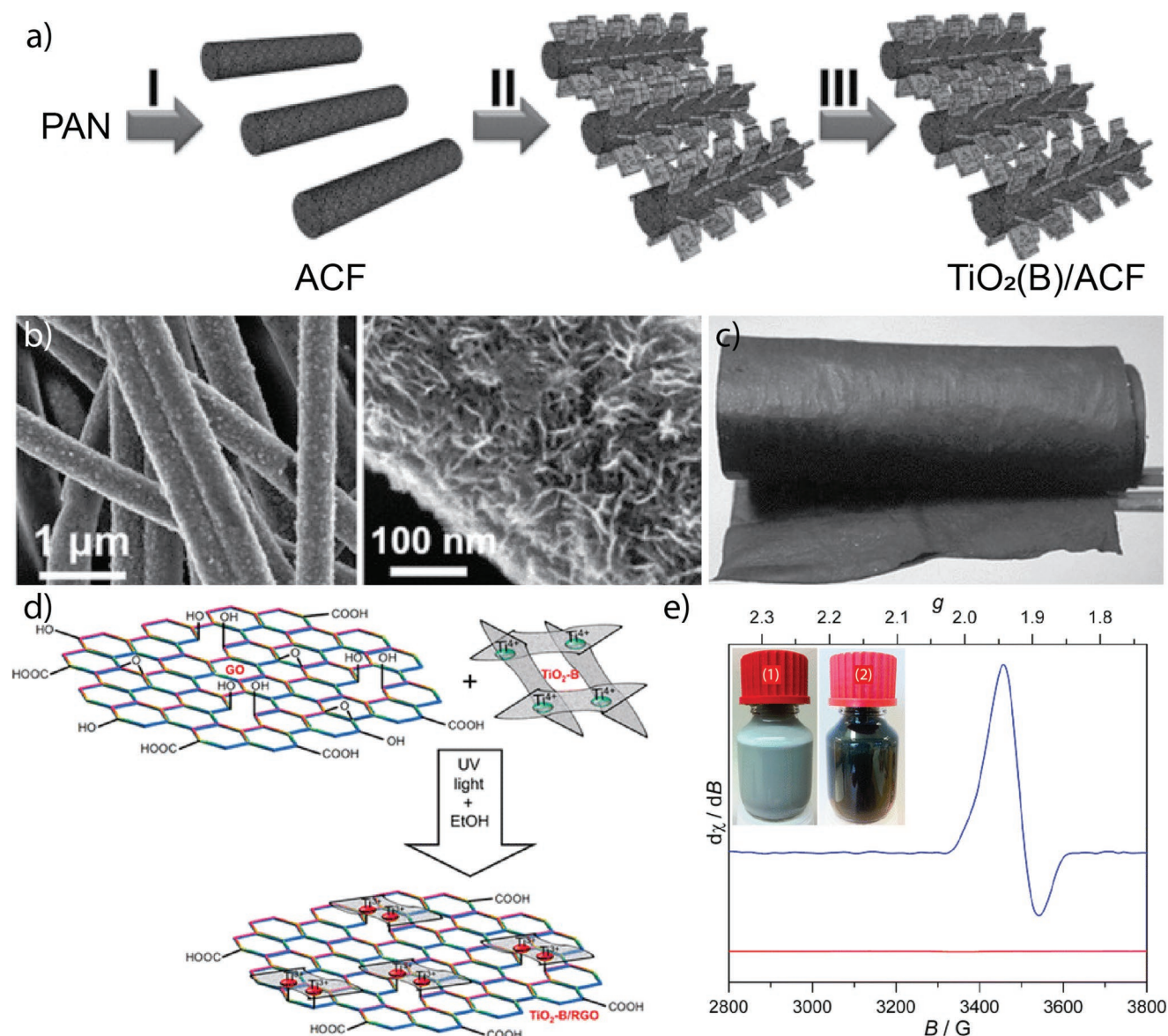


Figure 6. a) Schematic illustration of the formation of $\text{TiO}_2(\text{B})/\text{ACF}$ hybrid electrode; b) FESEM images of $\text{TiO}_2(\text{B})/\text{ACF}$ with different scale; c) photo of a rolled-up $\text{TiO}_2(\text{B})/\text{ACF}$ hybrid film. Reproduced with permission.^[105] Copyright 2013, Wiley-VCH. d) Synthesis of the $\text{TiO}_2(\text{B})/\text{rGO}$ hybrid nanostructure through photocatalytic reduction; e) EPR spectra of $\text{TiO}_2(\text{B})$ (red) and $\text{TiO}_2(\text{B})/\text{rGO}$ hybrid (blue). Inset: photographs of $\text{TiO}_2(\text{B})/\text{GO}$ in absolute ethanol (1) before and (2) after photoreduction. Reproduced with permission.^[112] Copyright 2014, American Chemical Society.

two-phase equilibrium reaction of $\text{TiO}_2(\text{B})$ crystal upon lithium insertion. The first and second phase transitions were located at the regions of 1.68 V ($\text{Li}_{\approx 0.1}\text{TiO}_2(\text{B})$)–1.57 V ($\text{Li}_{\approx 0.25}\text{TiO}_2(\text{B})$) versus Li/Li^+ and 1.57 V ($\text{Li}_{\approx 0.25}\text{TiO}_2(\text{B})$)–1.52 V ($\text{Li}_{\approx 0.5}\text{TiO}_2(\text{B})$) versus Li/Li^+ , respectively.

4.4. $\text{TiO}_2(\text{B})$ Nanosheets

Numerous studies about the $\text{TiO}_2(\text{B})$ nanosheets were reported from 2010 to 2015.^[97–106] In this period, The $\text{TiO}_2(\text{B})$ nanosheets were incorporated with oxygen vacancy or composited with electron conductive components including carbonaceous materials, and metal nanoparticles to further enhance the electrochemical

properties.^[11,91,105,107–112] In 2013, X. Lou et al. reported a kind of additive-free flexible film LIB anode where $\text{TiO}_2(\text{B})$ nanosheets were anchored on non-woven activated carbon fabric (ACF).^[105] The fabrication route is shown in **Figure 6a**. First, the ACF was fabricated by electrospinning, followed by thermal activation in CO_2 . Then, the $\text{TiO}_2(\text{B})$ nanosheets grew on the ACF via hydrolysis and condensation of the titanium precursor. Finally, the $\text{TiO}_2(\text{B})/\text{ACF}$ hybrid was annealed in the air in order to improve the crystallinity and purity of TiO_2 . Microscopically, the $\text{TiO}_2(\text{B})$ nanosheets were anchored on the surfaces of carbon nanofibers of the ACF (Figure 6b). In comparison, the as-prepared electrode exhibited great flexibility and could be rolled up easily at the macroscopic level (Figure 6c). This $\text{TiO}_2(\text{B})/\text{ACF}$ displayed

great cycling stability, maintaining a reversible capacity of 130 mAh g⁻¹ after 2000 cycles at a rate of 20 C (1 C = 335 mA g⁻¹). Moreover, it still delivered a capacity of 97 mAh g⁻¹ even at a high rate of 30 C. Such stable performance cannot achieve without the assistance of ACF. The existence of ACF not only allows easy access of lithium ions to the active material but also endows the electrode with good conductivity and high mechanical flexibility.

In 2014, V. Etacheri et al. bonded the TiO₂(B) nanosheets with the reduced graphene oxide (rGO) sheets through a photocatalytic reduction process.^[112] As shown in Figure 6d, the illumination with UV light-generated electrons and holes on the surface of the TiO₂(B) nanosheets, where the holes were consumed by the solvent, leaving accumulated electrons. The photo-generated electrons reduced Ti⁴⁺ to Ti³⁺ which could react with the carbon moieties within the graphene oxide to form the Ti-C bond, as confirmed by both the electron paramagnetic resonance (EPR) and X-ray photoelectron spectroscopy (XPS). In the EPR spectra (Figure 6e), the obvious EPR resonance at $g = 1.94$ of the TiO₂(B)/rGO hybrid indicated the existence of the surface Ti³⁺.^[113] The chemically bonded TiO₂(B)/rGO nanohybrid electrode exhibited significantly increased capacities and improved rate capabilities than the TiO₂(B)/rGO composite prepared by physically mixing. The effects of the additional anatase phase on the electrochemical properties of the TiO₂(B) nanosheets were also investigated by a few groups.^[94–95,114–115] It was found that the existence of the anatase phase could decrease the overall capacity of the composite, where the rate performance could also be compromised due to increased internal resistance. Annealing at a high temperature under the hydrogen atmosphere on the TiO₂(B) nanosheets was also performed to reduce the Ti⁴⁺ into Ti³⁺ and introduce oxygen vacancy into the lattice. The electron conductivity was increased to 2.79×10^{-3} S cm⁻¹ after the hydrogen treatment. The electrochemical performance, including the reversible capacity, rate capability, and cyclic stability was significantly improved compared to the pristine TiO₂(B) nanosheets.

4.5. TiO₂(B) Nanoparticles and Spheres

Macroporous/mesoporous structure and composition with the electron conductive carbon component could enhance the electrochemical performance of the TiO₂(B) particles in a synergistic way.^[116–119] H. Liu et al. prepared TiO₂(B) bare mesoporous particles via a multi-step process, where pristine mesoporous TiO₂ microspheres were firstly synthesized with ultrasonic spray pyrolysis method templated by silica particles.^[120] Further treatment in alkaline solution was applied to etch away the silica particles and convert the TiO₂ into sodium titanate, which was further transformed into hydrogen titanate through an ion exchange process by washing with the HCl solution. The subsequent dehydration treatment at 500 °C in argon atmosphere generated the TiO₂(B) mesoporous microspheres (Figure 7a). Due to its unique structure, a fast lithium ion transportation kinetics featured with a pseudocapacitive process was achieved, which was further coupled with facilitated electrolyte wetting on the electrode surface and compact particle packing. Excellent

high rate performance and stable cyclic stability were therefore observed.

Studies on the synthesis and structure formation mechanism of the solid TiO₂(B) particles were reported.^[121–123] Y. Ren et al. prepared super-small TiO₂(B) nanoparticles (Figure 7b) with a size of around 2.5 nm × 4.3 nm through a hydrothermal reaction process.^[37] Ti metal was first dissolved in a mixture of H₂O₂ and NH₃ in water. Then, glycolic acid was added to the solution to form a titanium glycolate complex. Through the subsequent hydrothermal treatment and final calcination in air, the TiO₂(B) nanoparticles were obtained. It was found that the lithiation capabilities of the TiO₂(B) at both high and low current densities were increased with reduced dimensions from the bulk TiO₂(B) to nanowires, nanotubes, and nanoparticles. The bulk TiO₂(B) exhibited the two-phase lithiation mechanism, but it became less distinct, and the discharge curves were featured with an increasing slope. The TiO₂(B) bare nanoparticles possessed similar gravimetric specific rate performance to that of the anatase TiO₂ nanoparticles with a size of 6 nm and composited with 45% of carbon by mass. It was noticed by the authors that the volumetric capacity of the TiO₂(B) at the current density higher than 1 A g⁻¹ was superior to the TiO₂(B) nanowires and nanotubes, and even the 6 nm-sized anatase nanoparticles. G. Zhu et al. first prepared the TiO₂(B) solid particle precursor of H₂Ti₃O₇ by a multi-step process, including mechanical ball milling between Na₂CO₃ and TiO₂, calcination, and hydrogenation with HCl solution.^[124] Based on the successful synthesis of the H₂Ti₃O₇ precursor, the structure transformation mechanism from the H₂Ti₃O₇ to the TiO₂(B) was investigated. It was found that the structure transformation was accompanied by a continuous interlayer water loss process, leading to the formation of a series of non-stoichiometric hydrogen titanate materials and ultimate TiO₂(B) particles. Besides the ball milling method, different alkaline titanates were used as the precursors to synthesize the TiO₂(B) particles. N. Takami et al. treated Na₂Ti₃O₇, K₂Ti₄O₉, and Cs₂Ti₅O₁₁ with proton exchange, followed by a dehydration process to synthesize the TiO₂(B) particles.^[36] Both the ion exchange protocol and dehydration process were optimized, where the chemical composition, morphology, phase purity, primitive cell volume, and corresponding electrochemical performance of the TiO₂(B) particles were systematically investigated. Besides the TiO₂(B) bare solid particles, composition with carbon was reported to enhance the electrochemical performance, where either carbon nanotube or polydopamine-based carbon was used.^[125,126]

Apart from the experimental work, fundamental mechanism studies on the TiO₂(B) nanoparticles were also reported. Y. G. Andreev et al. investigated the shape of the TiO₂(B) nanoparticles with the Debye formula and Monte Carlo optimization based on the powder diffraction data.^[127] Modeling at the atomic level and molecular dynamics simulation was introduced to reveal the reasons responsible for the shape and structures of the TiO₂(B) nanoparticles. It was found that the TiO₂(B) nanoparticles possessed a nearly ellipsoid shape according to the Debye studies, as displayed in Figure 7c,d. The modeling studies on the ensembles of all the ions in the

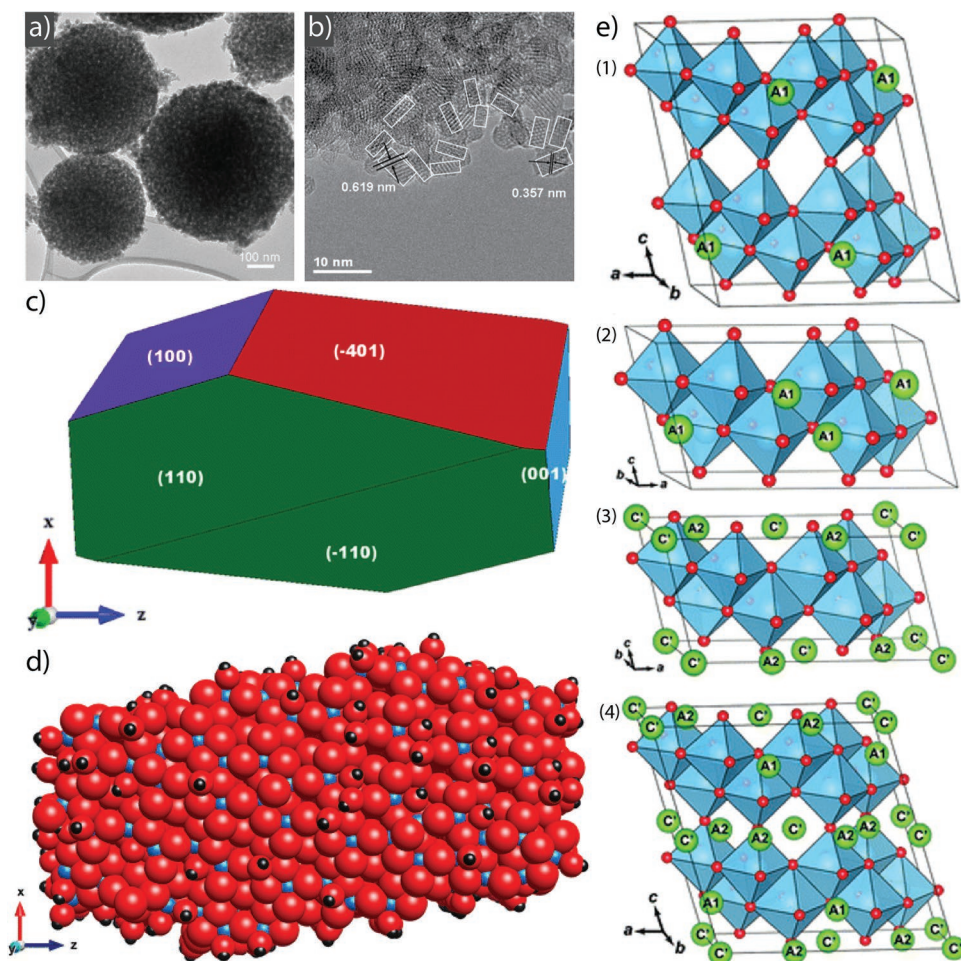


Figure 7. a) TEM image of mesoporous $\text{TiO}_2(\text{B})$ particle. Reproduced with permission.^[120] Copyright 2011, Wiley-VCH. b) High-resolution TEM image of $\text{TiO}_2(\text{B})$ nanoparticles. White boxes delineate primary (nano)particles within the agglomerates. Reproduced with permission.^[37] Copyright 2012, Wiley-VCH. c) Equilibrium shape of a hydroxylated crystalline particle of $\text{TiO}_2(\text{B})$ based on calculated surface energies; d) simulated ellipsoid shape of a hydroxylated nanoparticle (blue, red, and black spheres denote Ti, O, and H, respectively). Reproduced with permission.^[127] Copyright 2014, American Chemical Society. e) Ground-state structures for Li concentrations of e1) 0.25, e2) 0.5, e3) 0.75, and e4) 1.0. Reproduced with permission.^[128] Copyright 2012, American Chemical Society.

$\text{TiO}_2(\text{B})$ nanoparticle indicated that hydroxylation of the surface during the hydrothermal reaction was supposed to be a major reason for the formation of the ellipsoid shape, which was consistent with the results from the Debye refinement. The diffraction pattern generated from the atomic level simulation results was in good agreement with the experimental diffraction results. It was concluded that the surface and total energies of the $\text{TiO}_2(\text{B})$ nanoparticles were drastically modified by the surface hydroxyl functional groups, through which the surface strains and distortions of certain crystal facets were minimized. This conclusion was evidenced by the Debye refinement, where negligible strain values were observed. A. S. Dalton et al. elucidated the lithium insertion sites, voltage curves, and phase diagrams of the $\text{TiO}_2(\text{B})$ nanoparticles using first principle DFT calculations in combination with statistical mechanical methods.^[128] It was found that the lithium intercalation process was thermodynamically stable, with the Li/Ti uptake ratio up to 1.25. The phase diagram calculated at 300 K consisted of three first-order phase transitions, which

corresponded to changes in the favorable lithium intercalation sites with increasing Li/Ti ratios. In detail (Figure 7e), The A1 site was favored with the x value (Li concentration in a unit cell) not >0.5 . With the x value of 0.75, the A2 and C' sites were favorable for lithium insertion, and all the sites were in favor of lithium intercalation with further increasing x values. Correspondingly, a pronounced phase transition was observed with the x value changed from 0.5 to 0.75 because the lithium storage sites were modified from the A1 sites to the A2 and C' sites. Because the C' lithiation site was energetically stable and the A2 sites were fully occupied simultaneously with high Li/Ti uptake ratio, the (001) crystal facet of the $\text{TiO}_2(\text{B})$ nanoparticles should be fully occupied by the lithium ions. A. G. Dylla et al. calculated the different lithium intercalation mechanisms into the $\text{TiO}_2(\text{B})$ nanoparticles and nanosheets with the DFT+ U method.^[129] The calculation results showed that the A2 site near the equatorial TiO_6 octahedra was inserted by the lithium ions firstly in the $\text{TiO}_2(\text{B})$ nanoparticles, followed by the lithium insertion into the A1 site near

Table 2. Summary on representative studies about TiO₂(B) LIB anodes from 2010 to 2015 (ICE: initial Coulombic efficiency; *n*: the *n*th cycle; CD: current density).

Representative anode	Synthetic method	ICE	Charge capacity [mAh g ⁻¹] (<i>n</i> , CD)	Rate capacity [mAh g ⁻¹] (CD)	Remark	Ref.
Explosive stage: 2010–2015						
TiO ₂ (B)/G nanowires	hydrothermal treatment and self-scrolling	85%	153 (300, 3.35 A g ⁻¹)	135 (3.35 A g ⁻¹)	\	[78]
TiO ₂ (B)@SnO ₂ /C	hydrothermal reaction	43%	669 (67, 60 mA g ⁻¹)	282 (3 A g ⁻¹)	\	[82]
TiO ₂ (B) nanowires	followed from Ref. [26]	\	\	\	Li insertion sites study by powder neutron diffraction and DFT calculation	[83]
TiO ₂ (B) nanowires	hydrothermal reaction	\	\	\	nanosized effect on Li ⁺ insertion property in TiO ₂ (B) studied by XANES	[18]
TiO ₂ (B) nanotubes	hydrothermal process with stirring	≈76%	114 (10 000, 6.7 A g ⁻¹)	\	elongated bending nanotubes	[130]
TiO ₂ (B) nanotubes	followed from Ref. [30]	93%	≈200 (80, 20 mA g ⁻¹)	\	mitigation of irreversible capacity	[87]
TiO ₂ (B) nanorods	hydrothermal reaction	89%	≈80 (1000, 150 mA g ⁻¹)	60 (2 A g ⁻¹)	full-cell performance	[32]
TiO ₂ (B) nanorods	followed from Ref. [46]	\	\	\	in situ XRD study	[96]
TiO ₂ (B) nanosheet/ACF	electrospinning + hydrothermal process	75%	130 (2000, 6.7 A g ⁻¹)	97 (10 A g ⁻¹)	great flexibility	[105]
TiO ₂ (B) nanosheet/rGO	photocatalytic reduction	≈90%	≈240 (1000, 335 mA g ⁻¹)	≈200 (13.4 A g ⁻¹)	formation of Ti ³⁺ -C bonds chemically	[112]
TiO ₂ (B) microspheres	spray pyrolysis	77%	149 (5000, 3.35 A g ⁻¹)	115 (20 A g ⁻¹)	mesoporous structure	[120]
TiO ₂ (B) nanoparticles	hydrothermal reaction	\	\	≈120 (18 A g ⁻¹)	3 nm nanoparticles	[37]
TiO ₂ (B) nanoparticles	followed from Ref. [37]	\	\	\	study of TiO ₂ (B) shape by Debye formula and Monte Carlo optimization	[127]
TiO ₂ (B) nanoparticles	\	\	\	\	thermodynamics of Li in TiO ₂ (B) based on DFT and Monte Carlo simulations	[128]
TiO ₂ (B) nanoparticles	\	\	\	\	morphological dependence study of Li insertion in TiO ₂ (B) by DFT+ <i>U</i> calculations	[129]

the axial TiO₆ octahedra. The authors did not observe the lithium ion intercalation into the open channel C site. Unlike the TiO₂(B) nanoparticles, the TiO₂(B) nanosheets were first filled by the lithium ions in the C sites gradually, which was followed by the insertion into the A1 and A2 sites. The different lithium insertion mechanism was proposed to originate from the unusual elongated shape of the TiO₂(B) nanosheets along the *a* axis, where the interaction between the lithium ions in the sites of C and A2 was reduced. It was found that the lithiation potential and lithium intercalation degree were qualitatively consistent with the differential capacity profiles derived from the experimental results.

4.6. Summary of the Research Work from 2010–2015

TiO₂(B) emerged as a promising LIB anode before 2010. TiO₂(B) nanowires continued to attract increasing attention between 2010 and 2015. The structural types of TiO₂(B) anodes were generally the same as those in the last stage, mainly including nanowires, nanotubes, nanorods, nanosheets, and nanoparticles. In terms of composition, hybrid TiO₂(B) anodes gained much popularity, including TiO₂(B)/carbon, TiO₂(B)/metal oxide, and multi-phase TiO₂ composites. The second phases in hybrid TiO₂(B) anodes were beneficial for the enhancement of Li⁺ transport and mechanical properties, leading to stable electrochemical performance. As for the synthetic method, the hydrothermal treatment

of the TiO₂ nanoparticles in alkaline solution continued to be one of the major methods to fabricate nanostructured TiO₂(B) materials. Moreover, the theoretical investigations of TiO₂(B) also gained fruitful achievements during this period. With combined theoretical calculations and advanced characterizations, several fundamental problems of TiO₂(B) were well addressed, providing support for the optimization of electrochemical performance. The synthetic methods and electrochemical performance of representative studies about TiO₂(B) LIB anodes from 2010 to 2015 are summarized in Table 2.

5. Steady Development Stage of TiO₂(B) Anodes: Since 2015

The amount of the research work about TiO₂(B) anodes stayed unchanged from 2015 to the present. The experimental investigations on the synthesis and electrochemical properties of the nanostructured TiO₂(B) anode continued to be one of the central subjects of study during this time frame.^[131–136] A few theoretical studies were reported about the electrochemical mechanism of the lithiation and sodiation process of the TiO₂(B).^[137] Nanostructured TiO₂(B) with different morphologies were synthesized, which included porous particles, solid particles, nanotubes, nanowires (nanofibers), nanorods, and nanosheets.^[45,138–143] Due to the moderate electronic and ionic conductivities of the TiO₂(B), compositing with electron

conductive materials was performed such as graphene, carbon nanotube, and carbon derived from calcination of different precursors, metal particles, and electron conductive polymers.^[144] The incorporation of heteroatoms or oxygen vacancies into the TiO₂(B) lattice was also carried out to improve the electronic conductivity and electrochemical performance.^[23,145] The incorporation of high capacity materials of metal oxides, metal sulfides, and alloying metals effectively increased the overall capacities of the composites, where good cyclic stabilities were demonstrated as well.^[13,146,147] In general, the type of the electron conductive carbonaceous materials and metals for composition, the heteroatoms used for doping, and the high capacity components for composition were obviously increased compared to the previous time range. Besides, the studies on the TiO₂ were gradually shifted from LIB anodes to SIB anodes, which attracted considerable attention during this time range.^[3,148–150] The theoretical studies on the sodium intercalation of the TiO₂ based anodes were performed, which shed light on the fundamental electrochemical understanding of the sodiation/desodiation processes.^[137] The electrochemical performance measurements of the TiO₂(B) based anodes were not only based on the lithium half-cell configurations, but also the full cell batteries, which were instructive for the practical applications.^[151,152]

5.1. TiO₂(B) Nanowires/Nanofibers

The studies on the TiO₂(B) nanowires/nanofibers continued and were gradually extended from the LIBs to SIBs.^[21,153–161] S. Passerini et al. synthesized noodles-like TiO₂(B) nanowires secondary structure consisted of TiO₂(B) nanoparticles via a hydrothermal reaction in a mixed solvent of ethylene glycol and water using TiCl₃ as the precursor.^[154] The TiO₂(B) nanowires exhibited a different mechanism toward the sodiation process compared to the lithiation process. The TiO₂(B) nanoparticles were fully amorphized in the first cycle, which resulted in partial irreversible sodium storage. Both the cycling profile and electrochemical impedance spectroscopy suggested that the irreversible sodium storage was associated with the trap of the sodium ions within the particles and the unstable SEI layer. Despite the initial capacity loss, the TiO₂(B) nanowires exhibited a stable reversible capacity of around 100 mAh g⁻¹ and good rate performance as well. Y. Liu et al. compared the electrochemical performance of the anatase and TiO₂(B) nanowires as the sodium-ion battery anode.^[156] The experimental and calculation results indicated that sodium was intercalated into both anatase and TiO₂(B) nanowires. Even though the TiO₂(B) nanowires displayed higher initial sodiation capacities, similar reversible sodiation capacities corresponding to the composition of Na_{0.3}TiO₂ were exhibited by both the anatase and TiO₂(B) nanowires, which indicated the TiO₂(B) possessed more irreversible sodiation capacities. Further electrochemical performance tests showed that the anatase TiO₂ nanowires exhibited worse cyclic stability than the TiO₂(B) nanowires as the sodium-ion battery anode. It was likely due to the formation of the irreversible Na_xTiO₂ phase near the surface, where further sodium diffusion was blocked. Carbon composition and atomic doping were applied to improve the electron conductivity of the TiO₂(B) nanowires.

Graphene and carbon nanotube were utilized as the carbon matrix and the TiO₂(B) nanowires doped with carbon, nitrogen, and copper were reported.^[162–166] Additionally, introducing oxygen vacancies to tune the geometric structure and chemical properties of materials were widely applied in energy-storage devices.^[167–168] S. Li et al. developed a new concept to incorporate oxygen vacancy into TiO₂(B) nanowires induced by interfacial lattice strain through surface oxide coating.^[158] As shown in **Figure 8a**, according to the interfacial strain originated by the uneven volumetric shrinkage during the crystallization process, metal oxide heterostructures were designed by using TiO₂(B) as a model system. In the fabrication experiment (**Figure 8b**), oxide hydrate (H-TiO₂) nanofibers were first synthesized via a hydrothermal process. The metal oxide was subsequently coated on the surface of the H-TiO₂ nanofibers. After final calcination, the metal oxide-coated TiO₂(B) nanofibers were obtained, denoted as TiO₂(B)-M (M = Nb, Fe, Zr, V in this paper). During the heat treatment process, the generated interfacial strain could introduce oxygen defects into the interface between TiO₂(B) and metal oxide. The formation energy of the oxygen vacancy was significantly decreased under external strain, as suggested by both geometrical phase analysis and DFT simulation. Due to the existence of oxygen vacancy, the capacitive lithium storage was effectively increased, leading to exceptional rate capability compared to the oxygen-deficient TiO₂(B) prepared with the conventional air annealing process. Particularly, the as-prepared TiO₂(B)-Nb anode could retain a reversible capacity of ≈120 mAh g⁻¹ after 4000 cycles at 10 C (1 C = 335 mA g⁻¹), and also a capacity of 112 mAh g⁻¹ at 20 C. Besides the improvement of the electron conductivity, capacity increase by compositing with high theoretical capacity component was addressed, where VS₂, NiMoO₄, and anatase TiO₂ were used.^[169–171] The VS₂ possessed a 2D structure with intrinsic metallic nature, where the large inter-layer spacing was beneficial for lithium intercalation and high theoretical capacity.^[169] As a result, the TiO₂(B) nanowire/VSe₂ composite exhibited high reversible capacities and better rate performance than the bare TiO₂(B) nanowires.

Recently, A. Zhou et al. applied TiO₂(B) nanowires as the anode for aqueous LIBs, achieving low lithiation potential, high capacity, and high structural stability.^[172] The TiO₂(B) nanowires were fabricated by hydrothermal method and prepared as the anode to assemble a full cell with LiMnO₄ cathode and water-in-salt aqueous electrolyte. The LiMnO₄//TiO₂(B) full cell exhibited a wide working voltage range of 0.8–3 V and a high average discharge voltage of 2.35 V, due to the good match with the selected aqueous electrolyte. The full cell also displayed good cycling performance, maintaining a reversible capacity of 145 mAh g⁻¹ after 400 cycles at 200 mA g⁻¹ within 0.8–2.8 V. Besides, the full cell can deliver an energy density of about 150 Wh kg⁻¹ based on the total electrode mass.

5.2. TiO₂(B) Nanotubes

A few studies were reported about the TiO₂(B) nanotubes, where the bare TiO₂(B) nanotubes, tin-doped TiO₂(B) nanotube, TiO₂(B) nanotube/carbon composite, TiO₂(B) nanotube/TiO₂(B) nanoparticle, and TiO₂(B)/anatase nanotube-based composite

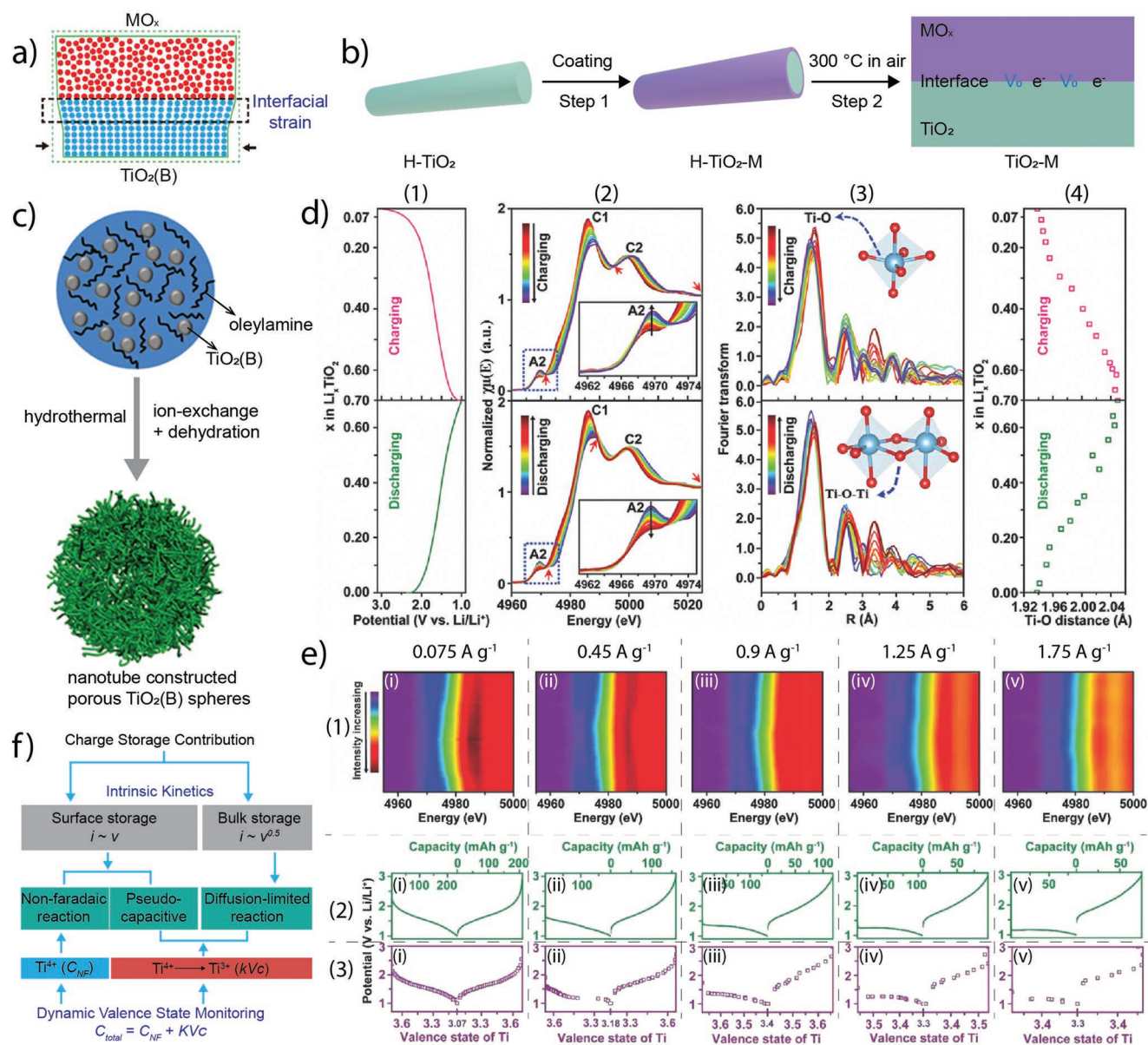


Figure 8. a) Proposed approach to construct oxide heterostructures for the introduction of interfacial lattice strain based on uneven volumetric shrinkage, promoting the generation of oxygen vacancies; b) schematic illustration of the synthetic process for the introduction of oxygen vacancies into TiO_2 through metal oxide surface coating based on the air-annealing process. Reproduced with permission.^[158] Copyright 2019, Wiley-VCH. c) Schematic illustration of the synthetic process of the $\text{TiO}_2(\text{B})$ material. Reproduced with permission.^[173] Copyright 2015, Springer Nature. d) In situ XAS studies of the $\text{TiO}_2(\text{B})$ nanotube electrode at a current density of 0.075 A g^{-1} . e) In situ dynamic valence state monitoring approach: e1) 2D contour plots of the Ti K-edge XANES spectra of the $\text{TiO}_2(\text{B})$ nanotube electrode at different current densities; e2) galvanostatic discharging/charging curves of the $\text{TiO}_2(\text{B})$ nanotube electrode; e3) evolution curves of Ti valence state of the $\text{TiO}_2(\text{B})$ nanotube electrode during the charging/discharging processes at different current densities. f) Schematic of the surface storage contribution of the $\text{TiO}_2(\text{B})$ nanotube electrode. Reproduced with permission.^[182] Copyright 2018, Wiley-VCH.

were addressed.^[173–181] Y. Cai et al. synthesized porous $\text{TiO}_2(\text{B})$ microspheres which were constructed by $\text{TiO}_2(\text{B})$ nanotubes through a hydrothermal reaction templated by oleylamine, as shown in Figure 8c.^[173] High reversible capacity with long cyclic life and excellent rate performance were demonstrated due to the synergistic effects from the $\text{TiO}_2(\text{B})$ crystallographic phase, porous structure, and inter-connected nanotube structure. $\text{TiO}_2(\text{B})$ nanotubes were in situ synthesized and anchored

onto the nitrogen-doped reduced graphene oxide sheet through a hydrothermal reaction with the presence of the graphene oxide.^[175] The incorporation of the reduced graphene oxide effectively improved the rate and cyclic performance because of the enhanced electron and ionic conductivities.

Up to now, various $\text{TiO}_2(\text{B})$ -based nanostructures and composites have demonstrated their great potential as advanced anode materials for LIBs/SIBs. Because of the large surface

area of nanostructured TiO₂(B) material, the surface storage mechanism can contribute a large part of the capacity. However, due to the complicated electrochemical reactions in nanostructured material, the origin and mechanism of surface storage for TiO₂(B) anode from non-faradaic and/or surface faradaic reactions were still unclear. In order to address this question, Y. Tang et al. developed in situ XAS and XRD measurements to monitor the Ti valence state changes during the charge–discharge process and further to investigate the origin and contribution of surface storage in the TiO₂(B) nanotube.^[182] First, as shown in Figure 8d1,d2, the absorption edge of Ti K-edge XANES, corresponding to the C1 and C2 crests, shifted toward lower-energy region during the discharging process. This indicated a continuous reduction of the average Ti valence state due to the transition of Ti⁴⁺ to Ti³⁺ in Li_xTiO₂(B) upon lithium insertion. In addition, as presented in Figure 8d3, the Fourier transformation of in situ Ti K-edge extended X-ray adsorption fine structure (EXAFS) oscillations provided the information about the local structure evolution (the radial distribution from individual shells of neighboring atoms around Ti atom). The intensity evolution of the peak related to the Ti–O bonds in the TiO₆ octahedra (around 1.5 Å) indicated that the TiO₆ octahedra increased the distortion during the lithium insertion process and then became less disordered when a lithiated phase of Li_{0.55}TiO₂(B) was reached. Besides, the length of Ti–O bonds was obtained by fitting the radial distribution data, as displayed in Figure 8d4. The results indicated a gradual expansion of the Ti–O bond length in the discharging process due to the continuous lithium insertion, resulting in the formation of larger Ti³⁺ (0.67 Å) instead of Ti⁴⁺ (0.61 Å). Moreover, in order to reveal the relationship between the evolution of Ti valence state and the charging/discharging rate, the in situ Ti K-edge XANES of TiO₂(B) nanotube anode was measured with different charging/discharging rates. As presented by the 2D contour plots of the XANES spectra in Figure 8e1, the Ti-K absorption edges exhibited an obvious shift toward lower-energy region during the discharging process at the current density of 0.075, 0.45, and 0.9 A g⁻¹. Then the absorption edges returned to the original locations in the later charging process, indicating a good reversibility of the TiO₂(B) nanotube structure during the cycling. Additionally, such variation of the Ti-K adsorption edges became less pronounced at high rates (1.25 and 1.75 A g⁻¹) due to the fast lithium insertion and extraction. Furthermore, based on the comprehensive analysis of in situ XANES data, the quantitative correlation between the evolution of Ti valence state and the charging/discharging rates was well established, as shown in the Figure 8e2,e3). The good agreement between the Ti valence state evolution curves and the charging/discharging curves at different rates indicated that the charging capacity and behavior were dominated by the faradaic reaction in the TiO₂(B) crystal. The changes of Ti valence state were observed throughout the charging/discharging process, indicating that the faradaic reaction also occurred during the surface storage. According to the understanding of Ti valence state evolution by in situ XAS and TiO₂(B) crystalline structure changes by in situ XRD, the authors developed the real-time correlation between the rate capability and dynamic Ti valence state based on CV measurements. As illustrated in Figure 8f, the charge storage contribution derives from surface

storage and bulk storage. The capacitive reaction on the electrode surface includes non-faradaic and surface faradaic (pseudocapacitive) reactions, while the capacitive reaction inside the electrode was related to the diffusion-limited reaction. From an electrochemical perspective, the total capacity was a combination of non-faradaic contribution (C_{NF}) and faradaic contribution (C_F) related to the Ti valence state change. Theoretically, C_{NF} was approximately constant at wide charging rates before reaching kinetic limit by electrostatic adsorption, while C_F was positively proportional to the valence state change (V_c), as shown in Equation (4).

$$C_{\text{total}} = C_{\text{NF}} + C_{\text{F}} = C_{\text{NF}} + kV_{\text{c}} \quad (4)$$

where *k* value was related to the theoretical capacity per valence state change. It was found that the titanium valence state changed continuously throughout the whole lithiation/delithiation process, no matter what the current densities were. The surface faradaic reaction modified the lithiation behavior because of increased lithium-ion insertion energy at the surface. The authors successfully made a quantitative analysis to elucidate the specific contribution of the non-faradaic and faradaic processes to the capacity by combining the in situ dynamic valence state monitoring and cyclic voltammetry test. It was indicated that the processes of the non-faradaic, pseudocapacitive, and diffusion contributed 11%, 60%, and 29% to the total capacity at a scanning rate of 2.0 mV s⁻¹.

5.3. TiO₂(B) Nanorods/Nanobelts

Although the synthetic methods of TiO₂(B) nanorods were not greatly updated in this stage, such as solid-state reaction and hydrothermal reaction, more secondary structures were established based on the nanorods.^[183,184] The precursor of K₂Ti₄O₉ was prepared by a solid-state reaction between TiO₂ and K₂CO₃, followed by proton exchange and dehydration treatment.^[183] The as-synthesized TiO₂(B) nanorods were assembled into spherical particles, which possessed high density and competitive volumetric capacity comparable to that of the graphite anode. Better rate performance and longer cyclic life were demonstrated by the spherical particles built by the TiO₂(B) nanorods compared to the TiO₂(B) nanorods disintegrated from the spherical particles. The improved electrochemical performance was confirmed by the reduced charge transfer resistance and passivating film resistance extracted from the electrochemical impedance spectroscopy. The electrochemical performance test based on the full cell configuration with a capacity of 2.8 Ah g⁻¹ revealed an energy density of 100 Wh kg⁻¹, a power density of 1800 W kg⁻¹ for 10 s pulse, and cyclic life of more than 3000 cycles, where the LiNi_{0.8}Co_{0.1}Mn_{0.1}O₂ was used as the cathode. The hydrothermal reaction was applied to synthesize 3D branched TiO₂ architectures (denoted as BTA) constructed by TiO₂(B) nanorods, where the relative mass ratio between water and diethylene glycol was found crucial to guide the assembly behavior of the TiO₂(B) nanorods.^[184] As displayed in Figure 9a, four 3D BTA samples were fabricated with different morphology. Among them, the BTA-4 sample exhibited the best electrochemical performance. Particularly, it could retain

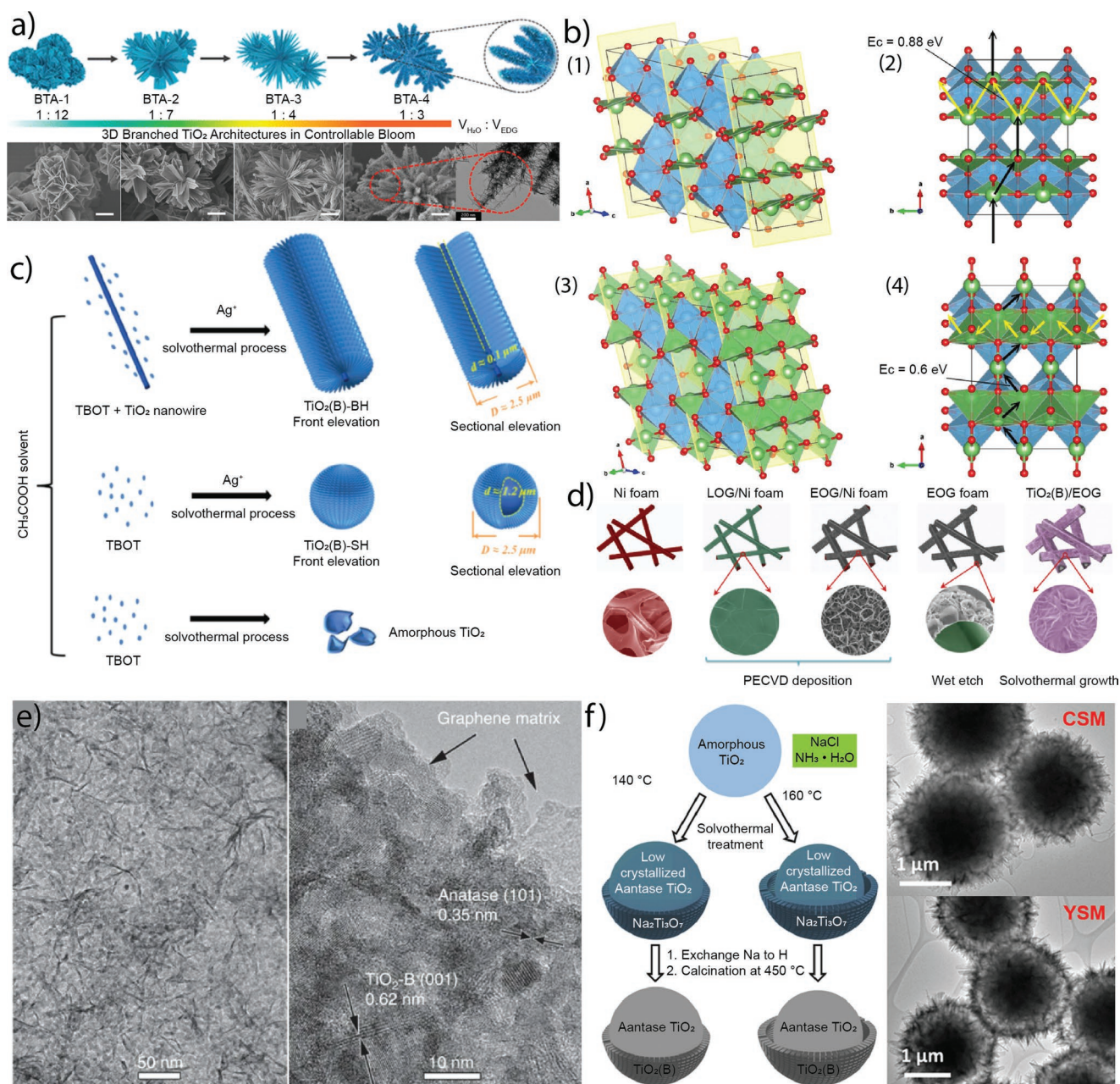


Figure 9. a) Schematic illustration of 3D branched TiO₂ architectures (BTA) in controllable bloom via precisely modulating volume ratio of H₂O and DEG, and corresponding SEM and TEM images. Reproduced with permission.^[184] Copyright 2016, American Chemical Society. b) Effect of crystal facets on lithium-ion intercalation in TiO₂(B): b1,b2) 1 × 2 × 2 supercell with the formula of Li₁₆Ti₃₂O₆₄ (A2); b3,b4) Li₂₄Ti₃₂O₆₄ (A2+C). The green, gray, and red spheres represent lithium, titanium, and oxygen, respectively. Reproduced under terms of the CC-BY license.^[191] Copyright 2020, The Authors published by Wiley-VCH. c) Illustrations of the distinguishing synthesis process of TiO₂ products. Reproduced with permission.^[197] Copyright 2016, Elsevier. d) Schematics illustrate the process used to produce the freestanding TiO₂(B)/EOG electrode. Reproduced with permission.^[203] Copyright 2016, Elsevier. e) TEM images of TiO₂(B)/G hybrid. Reproduced with permission.^[213] Copyright 2015, Macmillan Publishers Limited. f) Schematic representation of the synthesis of the mesoporous core-shell (CSM) and yolk-shell (YSM) anatase TiO₂/TiO₂(B) microspheres, and corresponding TEM images. Reproduced with permission.^[38] Copyright 2017, Wiley-VCH.

a reversible capacity of 195 mAh g⁻¹ after 200 cycles at a rate of 2 C (1 C = 170 mAh g⁻¹), and also a capacity of 123 mAh g⁻¹ at a high rate of 20 C. The remarkably enhanced electrochemical performance of the BTA-4 sample could be attributed to the formation of nanowire-coated dendrites which increased the specific surface area of the sample. Therefore, the accessibility

toward the electrolyte and reduced charge carrier transportation routes was improved significantly. Graphene and carbon nanotube were used to composite with the bare TiO₂(B) nanorods to improve the electron conductivity and electrochemical performance through the hydrothermal reaction.^[185,186] Besides, nitrogen doping was also introduced into the TiO₂(B) lattice

to enhance the electrochemical properties.^[187] Both the carbon composition and atomic doping were proved effective in increasing the reversible capacity and improving the rate performance as either lithium-ion or sodium-ion battery anodes.

Recently, TiO₂(B) nanobelts were also reported to act as high-performance anode materials for LIBs.^[188–191] Different strategies were applied to enhance the electrochemical performance of TiO₂(B) nanobelt anodes, including compositing with other materials,^[189] doping,^[190] and surface engineering.^[191] It has been demonstrated that anatase TiO₂ with exposed {001} facets could deliver better lithium storage performance than normal anatase TiO₂.^[192,193] Regarding TiO₂(B), Q. Wang et al. predicted by first-principle calculations that lithium ions prefer to intercalate through the {100} facets within the TiO₂(B) crystal.^[191] The energy barriers of lithium-ion diffusion in Li₁₆Ti₃₂O₆₄ (A2) and Li₂₄Ti₃₂O₆₄ (A2+C') were calculated and displayed in Figure 9b. As shown in Figure 9b1,b2, lithium ions occupy the A2 site and diffuse along with a zigzag pathway along the *b*-axis (yellow arrows) and zigzag-linear along *a*-axis (black arrows). The energy barrier of lithium ion diffusion was calculated as 0.88 eV. When the lithium ion further occupies the central C' site in the *ab* plane, as shown in Figure 9b3,b4, lithium ions can also diffuse along with a zigzag pathway along the *a*-axis (black arrows) via the central C' site, which lowers the diffusion energy barrier to 0.6 eV. It was concluded that lithium ions prefer to intercalate through the {100} facet of TiO₂(B) with relatively fast lithium-ion transportation instead of being adsorbed on {010} or {001} facets. Based on the calculation results, they fabricated TiO₂(B) nanobelts with exposed {100} facets via a topotactic transformation reaction from as-prepared H₂Ti₃O₇ nanobelts with significant {100} facet exposure. In order to further improve the electrochemical performance of TiO₂(B) nanobelts, a thin layer of copolymer (PEDOT-PSS, denoted as PP) was coated on the TiO₂(B) nanobelts to form a composite anode of TiO₂(B)@PP. As-prepared TiO₂(B)@PP anode exhibited a stable cycling performance over 1000 cycles at 335 mA g⁻¹ and also a good rate performance at a high current density of 10 A g⁻¹.

5.4. TiO₂(B) Nanosheets

TiO₂(B) nanosheet was regarded as a particularly promising anode for lithium-ion or sodium-ion batteries because of its unique 2D structures, which possessed rich active sites accessible for electrolyte and reduced charge carrier transportation lengths.^[194–196] X. Li et al. synthesized porous TiO₂(B) nanosheets, which were self-assembled into spherical particles (Figure 9c).^[197] The spherical particles were further stringed together by TiO₂ nanowires to form hierarchical bunched architectures. Fast pseudocapacitive process, accelerated charge carrier transportation, and good structure stability were demonstrated by the nanowire-nanosheets hierarchical architectures, leading to good electrochemical performance as the LIB anodes. It was accepted that the TiO₂(B) nanosheets exhibited good electrochemical kinetics due to the intrinsic electrochemically active crystallographic phase, enhanced accessibility toward electrolyte, and shortened charge carrier transportation length. However, further composition with carbon matrix including

polymer-based carbon and graphene was still an effective strategy to improve further the electrochemical performance as both lithium-ion and sodium-ion battery anodes.^[198–202] G. Ren et al. fabricated a 3D freestanding electrode, where the TiO₂(B) nanosheets were incorporated into the edge-oriented multilayer graphene foam (Figure 9d).^[203] The composites exhibited large reversible capacity, long cycling life, and high rate performance, which could be attributed to the edge-oriented graphene foam possessed fully exposed chemically active graphene edges and the orthogonal-oriented TiO₂(B) nanosheets with straight channels for enhanced electrolyte accessibility. In particular, this TiO₂(B)/G freestanding anode maintained a capacity retention of 82% after 12 000 cycles at 2.67 A g⁻¹. Moreover, this anode can deliver a reversible capacity of 49 mAh g⁻¹ at a current density as high as 40 A g⁻¹. X. Hu et al. composited TiO₂(B) nanosheets with nitrogen-rich mesoporous carbon matrix through a microwave irradiation process, where the TiO₂(B) nanosheets were in situ grown and bonded to the carbon matrix.^[198] The enhanced interaction at the interface between the TiO₂(B) nanosheets and carbon matrix increased reversible lithium insertion capability and improved electron conductivity as well, which was beneficial for accelerated charge carrier transportation. As a result, superior rate performance and long cycling life were exhibited by the TiO₂(B) nanosheets/nitrogen-rich mesoporous carbon composite with a safe operating voltage window of around 1.5 V. Besides carbon composition, doping with heteroatoms into the TiO₂(B) nanosheets was also reported.^[204] Y. Li et al. used the TiC as the precursor to prepare the carbon-doped TiO₂(B) by combing partial oxidation treatment and hydrothermal reaction together.^[205] It was found that carbon-doped TiO₂(B) nanosheets exhibited excellent rate performance and good cyclic stability due to the carbon doping and existence of multiple phase boundaries. Apart from the improvement of the electron conductivity, the capacity increase was another issue for the TiO₂(B) nanosheets, which was tackled by composition with SnO₂, NiO, Co₉S₈, Sn₃O₄, MoS₂, and anatase TiO₂ during this time frame.^[206–212] The solvothermal reaction was typically utilized to fabricate the composites, where the high capacity components were deposited onto the TiO₂(B) nanosheets. Further carbon composition was also applied, where the electrochemical kinetics was further enhanced due to the improved electron conductivity of the composites. The unique 2D structure of the TiO₂(B) nanosheets helped to alleviate adverse side effects associated with the volume expansion of the metal oxides/sulfides upon lithiation. A good interface contact between the TiO₂(B) nanosheets and metal oxide/sulfide nanoparticles was beneficial to retain electrochemically active charge carrier transportation routes over repeated cycles. Consequently, the composites exhibited increased reversible capacities and improved cyclic stabilities as either LIB or SIB anodes.

5.5. TiO₂(B) Nanoparticles and Spheres

Studies on the TiO₂(B) nanoparticles and spherical structures were mainly about the synthesis of hollow structures through hydrothermal reaction and composition with carbonaceous materials or metal oxides.^[14,39–41,214–217] The carbon matrix was derived from either bio-based materials or graphene

oxide.^[218–219] The oxides composited with the TiO₂(B) solid particles included Co₃O₄, SiO, anatase TiO₂ particles, and TiO₂(B) nanotubes as well.^[176,220–224] The TiO₂(B) solid particle-based composites were electrochemically active toward both lithium and sodium insertion.^[221,224] C. Chen et al. prepared TiO₂(B) nanoparticle/graphene composite (Figure 9e) with microwave-assisted hydrolysis and reduction method, which exhibited high rate capability and excellent cyclic stability as the sodium-ion battery anode originated from a pseudocapacitive process.^[213] The intimate contact between the graphene sheet and TiO₂(B) particles enhanced the sodium intercalation process by decreasing the diffusion energy barrier. H. Wei et al. fabricated mesoporous yolk-shell spheres composed of anatase TiO₂ core and TiO₂(B) shell through a sodium chloride assisted solvothermal reaction process.^[38] As shown in Figure 9f, amorphous TiO₂ was firstly treated by a hydrothermal process with different temperatures, forming the core-shell anatase TiO₂@Na₂Ti₃O₇ and yolk-shell anatase TiO₂@Na₂Ti₃O₇ microspheres, respectively. After an exchange reaction and calcination, the core-shell (CSM) anatase TiO₂/TiO₂(B) and yolk-shell (YCM) anatase TiO₂/TiO₂(B) were obtained. The hierarchical anatase TiO₂/TiO₂(B) composite particles exhibited high reversible capacity, excellent capacity retention over long cycles, and superior rate performance. It delivered a capacity of 182 mAh g⁻¹ at a high rate of 40 C (1 C = 168 mA g⁻¹) and kept a capacity retention of 98% after 500 cycles at a rate of 1 C. The TiO₂(B) shell provided electrochemically active sites to enhance the stability of the pseudocapacitive process. Besides, the mesoporous structure enhanced the electrolyte wetting, and also promoted the diffusion process of lithium ions. M. Sondergaard et al. investigated the phase transition and electrochemical performance of the anatase TiO₂/TiO₂(B) nanoparticle composite with different mass ratios of anatase TiO₂/TiO₂(B) and particle sizes.^[221] The in situ X-ray powder diffraction results indicated that the anatase phase became a dominant phase with the thermal annealing treatment above 375 °C. However, the phase transition could be inhibited by treating the precursors with NaOH before calcination, where the TiO₂(B) phase was retained with the annealing temperature up to 800 °C. The anatase TiO₂/TiO₂(B) composite particles exhibited good electrochemical performance compared to the literature results as the LIB anode. TiO₂(B) hollow particles were synthesized by a template-free hydrothermal reaction, where the Kirkendall effect played a key role in the formation of the hollow structures. Good electrochemical performance was observed due to the unique structure feature.^[215,225] L. Kong et al. used density functional theory calculations to investigate the effect of the oxygen vacancies on the electrochemical performance of the TiO₂(B) particles.^[226] The simulation results showed that the oxygen-deficient TiO₂(B) phase with a low lithium concentration of Li/Ti < 0.25 exhibited higher intercalation voltage and lower lithium transportation activation energy along the *b*-axis channel than the defect-free TiO₂(B) phase. Regarding the TiO₂(B) with the Li/Ti value of 1.0, the lithium de-intercalation process was favored due to the saturated oxygen-deficient phase and decreased lithium intercalation voltage. The bandgap of the defective TiO₂(B) was narrowed compared to the defect-free counterpart, where the electron conductivity was improved with increasing oxygen vacancy content.

5.6. Summary of the Research Work Since 2015

The research work since 2015 is featured with several characteristics. Experimental studies were dominant over this period, where composition and doping were widely used to enhance the electrochemical performance of the nanoscale TiO₂(B) anode. New strategies were addressed to introduce atomic defects into the TiO₂(B) lattice, which was accompanied by fundamental understanding. The application of the TiO₂(B) gradually shifted from LIBs to SIBs during this time range. In terms of TiO₂(B) nanowires and nanotubes, carbonaceous materials composition (graphene, carbon nanotube) and heteroatom doping (carbon, nitrogen, and copper) were applied to improve their electron conductivity. Various hierarchical structures were developed based on TiO₂(B) nanotubes and nanosheets. Studies on the TiO₂(B) micro/nanoparticles were focused on compositing with electron conductive carbonaceous materials or metal oxides bearing high capacities. Moreover, because of the superior synthesis methods, yolk-shell and hollow TiO₂(B) micro/nanoparticles were successfully fabricated in recent years. The synthetic methods and electrochemical performance of representative studies about TiO₂(B) LIB/SIB anodes since 2105 are summarized in Table 3.

6. Summary and Outlook

In summary, this review summarizes the research work on TiO₂(B) concerning both, LIB and SIB anodes from the 1980s to the present. A few general trends can be concluded based on the chronicle record of the studies over the last few decades, which are schematically presented in Figure 10.

First, TiO₂(B) was synthesized in 1980 with the structure identified by powder XRD and other techniques. Since its discovery, it was recognized capable of being electrochemically active toward lithiation with a theoretical Li/Ti ratio of 1.0. However, the preliminary results showed that the lithium uptake was only around 0.5, far below the theoretical value.

Second, the concept of nanomaterials science was introduced into the TiO₂(B) studies after 1990, where the TiO₂(B) nanowires were reported with exceptional lithium uptake of Li_{0.82}TiO₂, much higher than the values reported before. Mechanism studies and full battery performance tests were reported by the same group following this work. The work triggered vast studies on the nanoscale TiO₂(B) anodes. Other nanoscale morphologies such as nanotubes, nanorods, nanosheets, and nanoparticles were reported from 2000 to 2010. Advanced characterization techniques such as NMR were applied to elucidate the lithiation mechanism of the TiO₂(B) nanostructures. A few critical features regarding the lithiation process were revealed by combing the experimental and theoretical approaches. The pseudocapacitive process, lithium ion mobility, anisotropic lithium ion diffusion path, and specific lithium occupation sites of the nanoscale TiO₂(B) were successfully elucidated.

Third, strategies of composition and atomic doping were utilized between 2010 and 2015 to improve the electrochemical performance of the TiO₂(B) anodes with different morphologies. Besides the experimental studies, theoretical

Table 3. Summary on representative studies about TiO₂(B) LIB/SIB anodes since 2015 (ICE: initial Coulombic efficiency; *n*: the *n*th cycle; CD: current density).

Representative anode	Synthetic method	ICE	Charge capacity [mAh g ⁻¹] (<i>n</i> , CD)	Rate capacity [mAh g ⁻¹] (CD)	Remark	Ref.
TiO ₂ (B) nanowires	hydrolysis of TiCl ₃	41%	102 (70, 33.5 mA g ⁻¹)	50 (3.35 A g ⁻¹)	SIB performance	[154]
TiO ₂ (B) nanowires	hydrothermal process + heat treatment	\	120 (4000, 3.35 A g ⁻¹)	112 (6.7 A g ⁻¹)	oxygen vacancies introduced by interfacial strain between TiO ₂ (B) and MO _x	[158]
TiO ₂ (B)/VS ₂ nanowires	hydrothermal process	55%	365 (500, 335 mA g ⁻¹)	171 (3.35 A g ⁻¹)	\	[169]
TiO ₂ (B) nanowires	hydrothermal process	≈84%	145 (400, 200 mA g ⁻¹)	125 (0.8 A g ⁻¹)	LiMnO ₄ //TiO ₂ (B) full cell with aqueous electrolyte	[172]
TiO ₂ (B) nanotubes	hydrothermal process	\	154 (1000, 3.4 A g ⁻¹)	221 (3.4 A g ⁻¹)	hierarchical porous structure	[173]
TiO ₂ (B) nanotubes	hydrothermal process	\	\	\	study of surface storage in TiO ₂ (B) by in situ dynamic valence state monitoring	[182]
TiO ₂ (B) nanorods	solid-state reaction	\	≈220 (40, 200 mA g ⁻¹)	176 (4 A g ⁻¹)	microspheres assembled by TiO ₂ (B) nanorods	[183]
TiO ₂ (B) nanorods	hydrothermal process	72%	195 (200, 340 mA g ⁻¹)	123 (3.4 A g ⁻¹)	3D structure assembled by TiO ₂ (B) nanorods	[184]
TiO ₂ (B) nanobelts	hydrothermal process	100%	160 (1500, 335 mA g ⁻¹)	≈100 (10 A g ⁻¹)	{100} facets exposure	[191]
TiO ₂ (B) nanosheets	solvothermal process	80%	186 (1000, 1.67 A g ⁻¹)	159 (6.7 A g ⁻¹)	hierarchical structure based on TiO ₂ (B) nanosheets	[197]
TiO ₂ (B) nanosheets/G	PECVD + solvothermal process	\	≈170 (12 000, 2.67 A g ⁻¹)	49 (40 A g ⁻¹)	3D structure based on EOG foam	[198]
TiO ₂ (B) nanoparticles/G	microwave assisted hydrolysis	\	120 (4000, 500 mA g ⁻¹)	90 (12 A g ⁻¹)	SIB performance	[213]
TiO ₂ (B) microspheres	hydrothermal process + calcination	95%	260 (500, 168 mA g ⁻¹)	182 (6.7 A g ⁻¹)	yolk-shell structure	[38]
TiO ₂ (B) hollow nanoparticles	hydrothermal process	≈80%	≈230 (90, 84 mA g ⁻¹)	≈100 (1.68 A g ⁻¹)	application of Kirkendall effect	[215]

studies about the phase evolution induced by lithiation were reported to interpret the fundamental structure-performance correlations.

Fourth, studies about compositing and doping of TiO₂(B) continued to be the major stream from 2015 to the latest. However, the modified TiO₂(B) was increasingly explored as the SIB

anode, where studies on the sodiation behavior and mechanism were reported.

In order to in-depth understand the development trends of TiO₂(B) anode materials in different stages, we analyze and summarize the cycling and rate performance of various TiO₂(B) anode materials based on over 50 representative

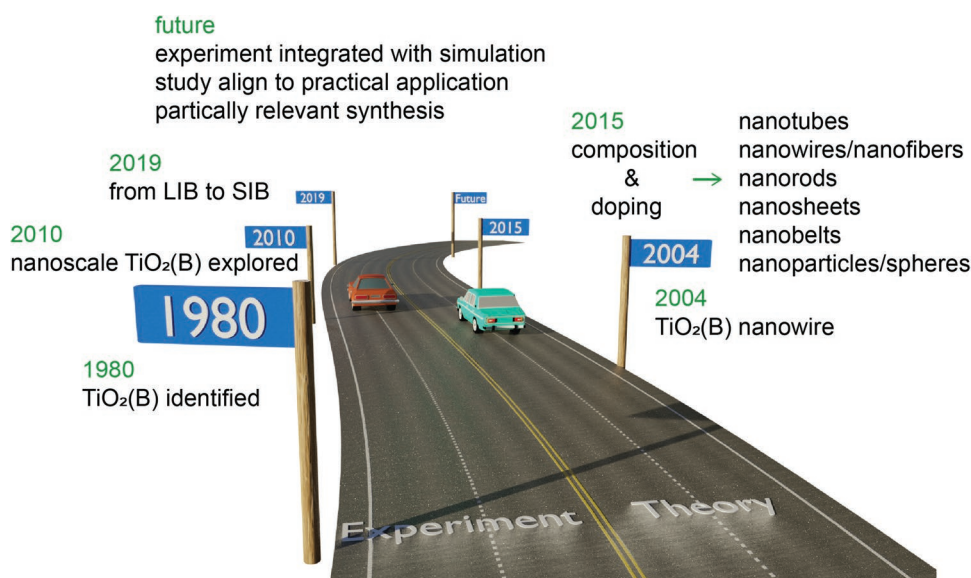


Figure 10. Schematic figure for the journey of the TiO₂(B) anode research toward practical application.

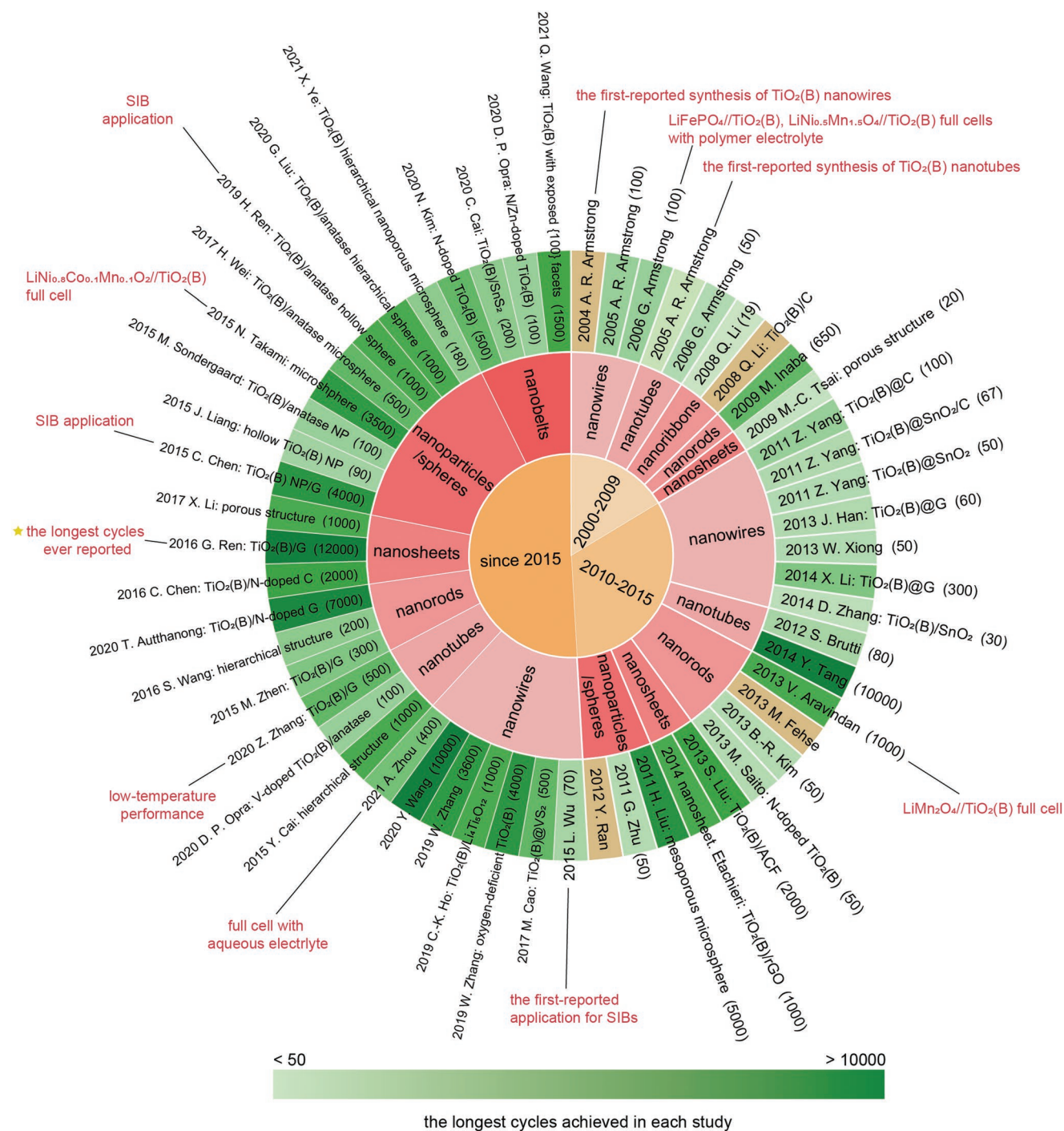


Figure 11. Statistics of the longest cycles achieved in the studies, which focus on $\text{TiO}_2(\text{B})$ anode materials reviewed in this work. In the outermost gradient green color mapping, the darker green represents the longer cycles achieved in the corresponding study. The brownish–yellow color represents that the cycling performance was not reported in the corresponding study. The exact cycling number reported in each study is presented in the bracket of each label.

studies mentioned in this review. As shown in **Figure 11**, we select the value of the longest cycles achieved in each study as a factor to evaluate the cycling performance of the corresponding $\text{TiO}_2(\text{B})$ anode material. In the outermost gradient green color mapping, the darker green represents the longer cycles achieved of $\text{TiO}_2(\text{B})$ anode material in the

corresponding study. Since the current densities applied for cycling measurements were different in different studies, the longest cycles achieved in each study cannot be considered as an absolute standard to judge the cycling performance of corresponding $\text{TiO}_2(\text{B})$ anode material. However, we think this evaluation method is still reasonable and meaningful because

the value of the longest cycles achieved in each study reflects the extreme cycling performance of the corresponding $\text{TiO}_2(\text{B})$ anode material at a tolerable current density. In Figure 10, it is obvious that in general the color of blocks distributed in the stage since 2015 is darker than those in the stage 2010–2015 and the stage 2000–2009. Meanwhile, the color of blocks in the stage 2010–2015 is also darker than those in the stage 2000–2009. This trend indicates that the average cycling performance of $\text{TiO}_2(\text{B})$ anode materials gained great improvements with time. The first breakthrough appeared at about 2011–2014 when the cycle limit of $\text{TiO}_2(\text{B})$ anode material was lifted from a hundred level to a thousand level even to a dozens-of-thousand level. This could be attributed to more delicate nanostructures than before, such as elongated nanotubes, porous, and hierarchical structures, which benefits to enhance the diffusion of lithium ions and the structural stability.^[86,105,120] Since 2015, more and more $\text{TiO}_2(\text{B})$ anode materials delivered stable cycling performance over 1000 cycles. To our best knowledge, the most cycles of $\text{TiO}_2(\text{B})$ anode material was 12 000, achieved by G. Ren et al. in 2016.^[203]

Regarding the rate performance, we also apply the same statistical approach to collect the highest current density achieved in each study mentioned above, evaluating the rate performance of various $\text{TiO}_2(\text{B})$ anode materials, as presented in **Figure 12**. In the outermost gradient blue color mapping, the darker blue represents the higher current density applied for $\text{TiO}_2(\text{B})$ anode material in the corresponding study. Similar to the trend presented in the cycling performance, the blue blocks generally become darker and darker with time evolution, indicating the better and better rate performance. A great improvement of the rate performance of $\text{TiO}_2(\text{B})$ anode materials was also achieved at about 2011–2014, when the highest current density applied for $\text{TiO}_2(\text{B})$ anode materials was improved from below 2 A g^{-1} to over 10 A g^{-1} even to 20 A g^{-1} . This indicates that the optimization strategies mentioned above can enhance both the cycling and rate performance of $\text{TiO}_2(\text{B})$ anode materials. The ever-reported highest current density applied for $\text{TiO}_2(\text{B})$ anode materials, 40 A g^{-1} , was also achieved by G. Ren et al. in 2016. From an overview of Figure 10 and Figure 11, it is obvious that compositing $\text{TiO}_2(\text{B})$ with carbonaceous materials is an effective strategy to enhance the cycling and rate performance of $\text{TiO}_2(\text{B})$ anodes simultaneously. Moreover, some pure $\text{TiO}_2(\text{B})$ material with delicate nanostructure design (such as porous structure, elongated 1D structure, and hierarchical structure) and surface engineering (such as the introduction of oxygen vacancy and facets exposure) can also greatly improve the electrochemical performance of $\text{TiO}_2(\text{B})$ anodes.

Based on a comprehensive review of the research in the past and understanding of the technology development of the LIB and SIB industry, a few directions may be particularly explored regarding the future research work on $\text{TiO}_2(\text{B})$ anodes.

i) It is essential to combine theoretical and experimental studies to advance the fundamental understanding and the practical material development of the $\text{TiO}_2(\text{B})$ anode. The reviewed work indicates that theoretical work has been mainly addressed between 2000 and 2015. The research efforts in the last few years have been heavily focused on materials synthesis and property testing such as morphol-

ogy tuning, composition, and doping. Theoretical investigations on the as-synthesized systems have been very limited. However, fundamental insights about the as-synthesized $\text{TiO}_2(\text{B})$ are crucial to guide the design and synthesis of new high-performance $\text{TiO}_2(\text{B})$ anodes.

- ii) It is necessary to align the research work to the practical requirements of the $\text{TiO}_2(\text{B})$ anode in real applications. For example, most of the reported studies so far were limited to the half-cell test. However, full-cell performance is particularly instructive for practical applications. It would make sense to identify and tackle the issues of the $\text{TiO}_2(\text{B})$ anode generated from the full-cell configuration. Studies beyond morphology control, composition, and atomic doping can also be important to advance the practical application of the $\text{TiO}_2(\text{B})$ anodes. The topics such as the interaction between the organic electrolyte and $\text{TiO}_2(\text{B})$ particles at the interface, rationality for the combination of $\text{TiO}_2(\text{B})$ anode and different cathodes, improvement of initial Coulombic efficiency, and maintaining high capacity retention over long cycles in full-cell tests, are critical to realizing practical application of the $\text{TiO}_2(\text{B})$ anode.
- iii) There is still great space to develop scalable, cost-effective, and reliable synthetic methods to produce high-performance $\text{TiO}_2(\text{B})$ anodes. So far, many synthetic methods have been addressed to synthesize $\text{TiO}_2(\text{B})$ anodes with good control over crystallinity, composition, morphology, and defects. However, most of the synthetic methods were not further optimized according to the practical requirements for the large-scale $\text{TiO}_2(\text{B})$ anode synthesis.
- iv) In order to achieve high-performance $\text{TiO}_2(\text{B})$ -based LIBs/SIBs, it is not enough to only develop $\text{TiO}_2(\text{B})$ anodes. It is necessary to promote the studies on the electrolytes and related additives for $\text{TiO}_2(\text{B})$ anodes. A key issue, which needs to be addressed, is suppressing the formation of hydrofluoric acid by the hydrolysis of the electrolyte. The formed hydrofluoric acid could react with the $\text{TiO}_2(\text{B})$ anode, leading to a damage of the $\text{TiO}_2(\text{B})$ structure and finally a decay of electrochemical performance.
- v) An appropriate binder also plays an important role to ensure good performance release and maintenance of $\text{TiO}_2(\text{B})$ anodes. Water-soluble binders, such as styrene butadiene rubber (SBR) and sodium sodium carboxyl methyl cellulose (NaCMC), have been widely used in the graphite anode system.^[227,228] However, it may not be the best option for the $\text{TiO}_2(\text{B})$ anode. Therefore, further studies on developing new water-soluble binders for $\text{TiO}_2(\text{B})$ regarding the engineering application and mechanism understanding about the coating and electrochemical processes are crucial to promoting the real application of $\text{TiO}_2(\text{B})$ -based LIBs/SIBs.
- vi) With the overview of various $\text{TiO}_2(\text{B})$ anodes and corresponding development trends, we believe that $\text{TiO}_2(\text{B})$ /carbon composite would be one of the most promising systems for future practical applications in LIBs/SIBs. Promoting a kind of $\text{TiO}_2(\text{B})$ -based anode material to the real application should find a great balance point among the comparable electrochemical performance, facile and scalable fabrication method, and the cost of raw materials and production. Compared to other $\text{TiO}_2(\text{B})$ nanomaterials in this review, $\text{TiO}_2(\text{B})$ nanoparticles have the simplest structure, leading to achieve the

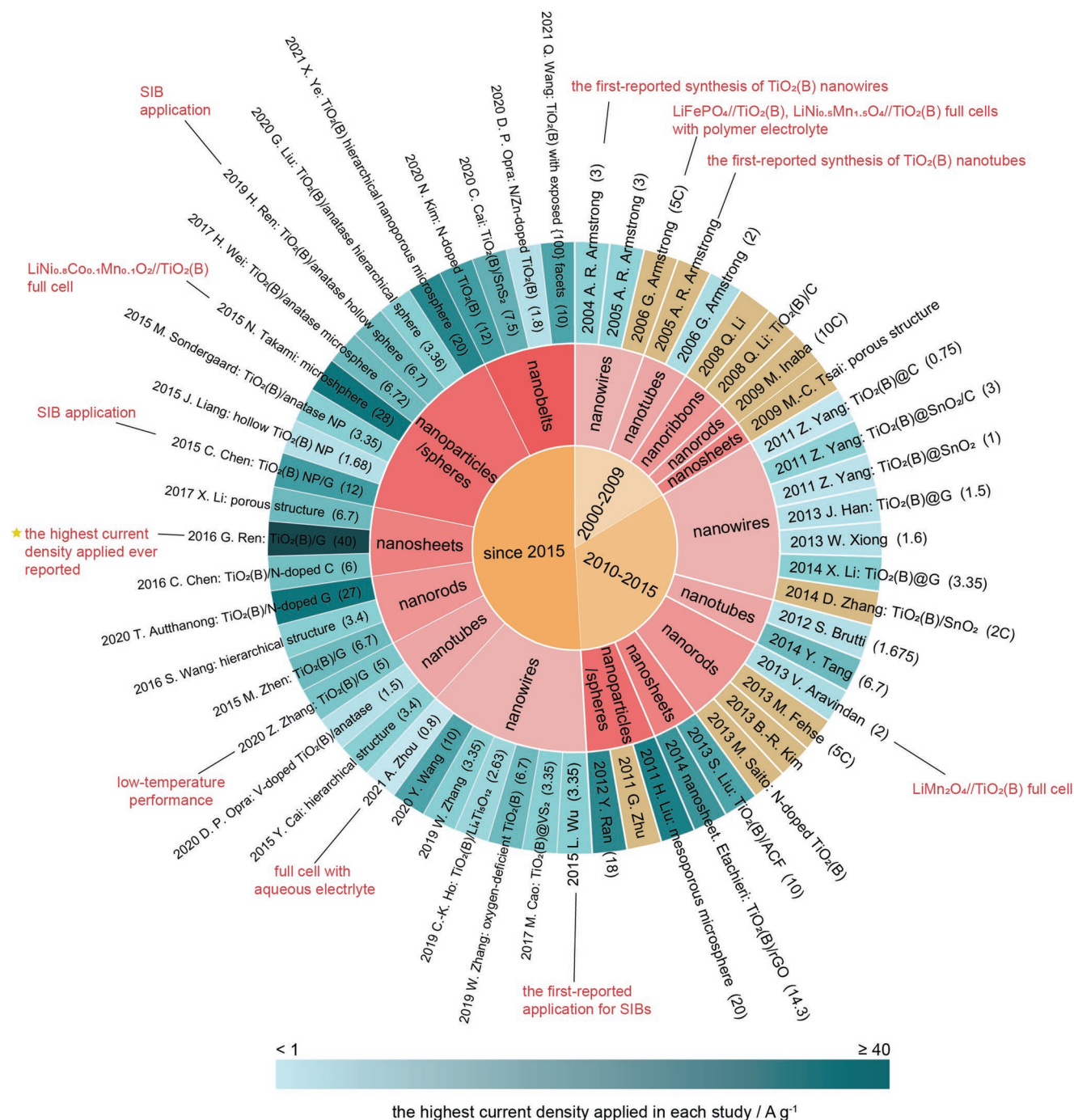


Figure 12. Statistics of the highest current density (unit: $A\ g^{-1}$) applied in the studies, which focus on $TiO_2(B)$ anode materials reviewed in this work. In the outermost gradient blue color mapping, the darker blue represents the higher current density applied in the corresponding study. The brownish-yellow color represents that the rate performance was not reported or the specific value of current density was not mentioned in the corresponding study. The exact highest current density applied in each study is presented in the bracket of each label.

easy and large-scale production. In addition, by compositing with carbonaceous materials and other optimization strategies (such as doping), both cycling and rate performance of some $TiO_2(B)$ nanoparticles-based anodes have reached a very competitive level, as shown in Figures 11 and 12. Therefore, realizing practical applications of $TiO_2(B)$ nanoparticles-based anodes can be expected in near future.

Acknowledgements

S.L., X.W., and R.Q. contributed equally to this work. This research is supported by the National Natural Science Foundation of China (52061135110, 21773279, 22075305), Natural Science Foundation of Zhejiang Province (LD22E020003), Zhejiang Province Public Welfare Technology Application Research Project (LGG19B010001), Ningbo Municipal Natural Science Foundation (202003N4349), the Key Research

Program of the Chinese Academy of Sciences (ZDRW_CN_2020-1), and the Ningbo Science and Technology Innovation 2025 Major Project (2019B10050, 2019B10113, 2020Z024, 2020Z101, 2020Z025), and Key Laboratory of Bio-based Polymeric Materials of Zhejiang Province. S.L. acknowledges the China Scholarship Council (CSC) for funding. P.M.-B. acknowledges funding by the International Research Training Group 2022 Alberta/Technical University of Munich International Graduate School for Environmentally Responsible Functional Hybrid Materials (ATUMS). X. H. acknowledges support for the EPFL.

Open access funding enabled and organized by Projekt DEAL.

Conflict of Interest

The authors declare no conflict of interest.

Keywords

bronze-phase titanium dioxide, chronicle perspective, electrochemical performance, lithium-ion battery anode, sodium-ion battery anode

Received: February 11, 2022

Revised: March 22, 2022

Published online: April 21, 2022

-
- [1] J. M. Tarascon, M. Armand, *Nature* **2001**, 414, 359.
 [2] A. Yoshino, *Angew. Chem., Int. Ed.* **2012**, 51, 5798.
 [3] D. Larcher, J. M. Tarascon, *Nat. Chem.* **2015**, 7, 19.
 [4] N. Loeffler, D. Bresser, S. Passerini, M. Copley, *Johns Matthey Technol. Rev.* **2015**, 59, 34.
 [5] D. V. Bavykin, J. M. Friedrich, F. C. Walsh, *Adv. Mater.* **2006**, 18, 2807.
 [6] S. Liang, X. Wang, Y.-J. Cheng, Y. Xia, P. Müller-Buschbaum, *Energy Storage Mater.* **2022**, 45, 201.
 [7] X. Chen, S. S. Mao, *Chem. Rev.* **2007**, 107, 2891.
 [8] U. Balachandran, N. Eror, *J. Solid State Chem.* **1982**, 42, 276.
 [9] W. Ma, Z. Lu, M. Zhang, *Appl. Phys. A* **1998**, 66, 621.
 [10] A. G. Dylla, G. Henkelman, K. J. Stevenson, *Acc. Chem. Res.* **2013**, 46, 1104.
 [11] H. Huang, J. Fang, Y. Xia, X. Tao, Y. Gan, J. Du, W. Zhu, W. Zhang, *J. Mater. Chem. A* **2013**, 1, 2495.
 [12] Z. Liu, Y. G. Andreev, A. R. Armstrong, S. Brutti, Y. Ren, P. G. Bruce, *Prog. Nat. Sci.: Mater. Int.* **2013**, 23, 235.
 [13] Y. Liu, Y. Yang, *J. Nanomater.* **2016**, 2016, 8123652.
 [14] M. Fehse, E. Ventosa, *ChemPlusChem* **2015**, 80, 785.
 [15] Z. Chen, I. Belharouak, Y. K. Sun, K. Amine, *Adv. Funct. Mater.* **2013**, 23, 959.
 [16] D. L. Gao, Y. L. Wang, J. Kong, F. Huo, S. F. Wang, H. Y. He, S. J. Zhang, *Phys. Chem. Chem. Phys.* **2019**, 21, 17985.
 [17] Q. Zhang, P. Kaghazchi, *J. Phys. Chem. C* **2016**, 120, 22163.
 [18] T. Okumura, T. Fukutsuka, A. Yanagihara, Y. Orikasa, H. Arai, Z. Ogumi, Y. Uchimoto, *Chem. Mater.* **2011**, 23, 3636.
 [19] N. Yabuuchi, K. Kubota, M. Dahbi, S. Komaba, *Chem. Rev.* **2014**, 114, 11636.
 [20] S. Liang, Y. J. Cheng, J. Zhu, Y. Xia, P. Müller-Buschbaum, *Small Methods* **2020**, 4, 2000218.
 [21] J. Lee, J. K. Lee, K. Y. Chung, H.-G. Jung, H. Kim, J. Mun, W. Choi, *Electrochim. Acta* **2016**, 200, 21.
 [22] G.-N. Zhu, Y.-G. Wang, Y.-Y. Xia, *Energy Environ. Sci.* **2012**, 5, 6652.
 [23] X. Chen, L. Liu, F. Huang, *Chem. Soc. Rev.* **2015**, 44, 1861.
 [24] M. Dahl, Y. Liu, Y. Yin, *Chem. Rev.* **2014**, 114, 9853.
 [25] L. Liu, X. Chen, *Chem. Rev.* **2014**, 114, 9890.
 [26] A. R. Armstrong, G. Armstrong, J. Canales, P. G. Bruce, *Angew. Chem., Int. Ed.* **2004**, 43, 2286.
 [27] Y. Guo, N.-H. Lee, H.-J. Oh, C.-R. Yoon, K.-S. Park, H.-G. Lee, K.-S. Lee, S.-J. Kim, *Nanotechnology* **2007**, 18, 295608.
 [28] D. V. Bavykin, V. N. Parmon, A. A. Lapkin, F. C. Walsh, *J. Mater. Chem.* **2004**, 14, 3370.
 [29] A. R. Armstrong, G. Armstrong, J. Canales, P. G. Bruce, *J. Power Sources* **2005**, 146, 501.
 [30] G. Armstrong, A. R. Armstrong, J. Canales, P. G. Bruce, *Chem. Commun.* **2005**, 19, 2454.
 [31] K. Pan, Y. Dong, C. Tian, W. Zhou, G. Tian, B. Zhao, H. Fu, *Electrochim. Acta* **2009**, 54, 7350.
 [32] V. Aravindan, N. Shubha, Y. L. Cheah, R. Prasanth, W. Chuileng, R. R. Prabhakar, S. Madhavi, *J. Mater. Chem. A* **2013**, 1, 308.
 [33] D. Wu, J. Liu, X. Zhao, A. Li, Y. Chen, N. Ming, *Chem. Mater.* **2006**, 18, 547.
 [34] G. Xiang, T. Li, J. Zhuang, X. Wang, *Chem. Commun.* **2010**, 46, 6801.
 [35] M. Kobayashi, V. V. Petrykin, M. Kakihana, K. Tomita, M. Yoshimura, *Chem. Mater.* **2007**, 19, 5373.
 [36] Y. Harada, K. Hoshina, H. Inagaki, N. Takami, *Electrochim. Acta* **2013**, 112, 310.
 [37] Y. Ren, Z. Liu, F. Pourpoint, A. R. Armstrong, C. P. Grey, P. G. Bruce, *Angew. Chem., Int. Ed.* **2012**, 51, 2164.
 [38] H. Wei, E. F. Rodriguez, A. F. Hollenkamp, A. I. Bhatt, D. Chen, R. A. Caruso, *Adv. Funct. Mater.* **2017**, 27, 1703270.
 [39] H. Ren, R. B. Yu, J. Qi, L. J. Zhang, Q. Jin, D. Wang, *Adv. Mater.* **2019**, 31, 1805754.
 [40] G. L. Liu, H. H. Wu, Q. Q. Meng, T. Zhang, D. Sun, X. Y. Jin, D. L. Guo, N. T. Wu, X. M. Liu, J. K. Kim, *Nanoscale Horiz.* **2020**, 5, 150.
 [41] X. Z. Ye, H. R. Hu, H. Xiong, Y. Wang, J. F. Ye, *J. Colloid Interface Sci.* **2021**, 600, 530.
 [42] T. Froeschl, U. Hoermann, P. Kubiak, G. Kucerova, M. Pfanzelt, C. K. Weiss, R. J. Behm, N. Huesing, U. Kaiser, K. Landfester, M. Wohlfahrt-Mehrens, *Chem. Soc. Rev.* **2012**, 41, 5313.
 [43] J. Tian, Z. Zhao, A. Kumar, R. I. Boughton, H. Liu, *Chem. Soc. Rev.* **2014**, 43, 6920.
 [44] Z. Yang, D. Choi, S. Kerisit, K. M. Rosso, D. Wang, J. Zhang, G. Graff, J. Liu, *J. Power Sources* **2009**, 192, 588.
 [45] M. Abdullah, S. K. Kamarudin, *Renewable Sustainable Energy Rev.* **2017**, 76, 212.
 [46] R. Marchand, L. Brohan, M. Tournoux, *Mater. Res. Bull.* **1980**, 15, 1129.
 [47] M. Tournoux, R. Marchand, L. Brohan, *Prog. Solid State Chem.* **1986**, 17, 33.
 [48] B. Zachaerchristiansen, K. West, T. Jacobsen, S. Atlung, *Solid State Ion* **1988**, 28, 1176.
 [49] J. F. Banfield, D. R. Veblen, D. J. Smith, *Am. Mineral.* **1991**, 76, 343.
 [50] J. F. Banfield, D. R. Veblen, *Am. Mineral.* **1992**, 77, 545.
 [51] T. P. Feist, P. K. Davies, *J. Solid State Chem.* **1992**, 101, 275.
 [52] A. R. Armstrong, G. Armstrong, J. Canales, R. Garcia, P. G. Bruce, *Adv. Mater.* **2005**, 17, 862.
 [53] G. Armstrong, A. R. Armstrong, P. G. Bruce, P. Reale, B. Scrosati, *Adv. Mater.* **2006**, 18, 2597.
 [54] S. Pavasupree, Y. Suzuki, S. Yoshikawa, R. Kawahata, *J. Solid State Chem.* **2005**, 178, 3110.
 [55] M. Zukalova, M. Kalbac, L. Kavan, I. Exnar, M. Graetzel, *Chem. Mater.* **2005**, 17, 1248.
 [56] M. Wilkening, J. Heine, C. Lyness, A. R. Armstrong, P. G. Bruce, *Phys. Rev. B* **2009**, 80, 064302.
 [57] M. Wilkening, C. Lyness, A. R. Armstrong, P. G. Bruce, *J. Phys. Chem. C* **2009**, 113, 4741.
 [58] G. Armstrong, A. R. Armstrong, J. Canales, P. G. Bruce, *Electrochem. Solid-State Lett.* **2006**, 9, A139.

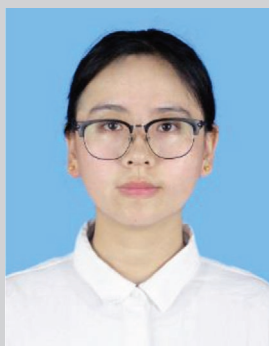
- [59] E. Morgado, Jr., P. M. Jardim, B. A. Marinkovic, F. C. Rizzo, M. A. S. De Abreu, J. L. Zotin, A. S. Araujo, *Nanotechnology* **2007**, *18*, 495710.
- [60] M. Inaba, Y. Oba, F. Niina, Y. Murota, Y. Ogino, A. Tasaka, K. Hirota, *J. Power Sources* **2009**, *189*, 580.
- [61] Q. Li, J. Zhang, B. Liu, M. Li, R. Liu, X. Li, H. Ma, S. Yu, L. Wang, Y. Zou, Z. Li, B. Zou, T. Cui, G. Zou, *Inorg. Chem.* **2008**, *47*, 9870.
- [62] M.-C. Tsai, J.-C. Chang, H.-S. Sheu, H.-T. Chiu, C.-Y. Lee, *Chem. Mater.* **2009**, *21*, 499.
- [63] M. Kobayashi, V. V. Petrykin, M. Kakihana, *Chem. Mater.* **2007**, *19*, 5373.
- [64] Q. Li, J. Zhang, B. Liu, M. Li, S. Yu, L. Wang, Z. Li, D. Liu, Y. Hou, Y. Zou, B. Zou, T. Cui, G. Zou, *Cryst. Growth Des.* **2008**, *8*, 1812.
- [65] C. Arrouvel, S. C. Parker, M. S. Islam, *Chem. Mater.* **2009**, *21*, 4778.
- [66] D. Panduwina, J. D. Gale, *J. Mater. Chem.* **2009**, *19*, 3931.
- [67] D. Fattakhova-Rohlfing, A. Zaleska, T. Bein, *Chem. Rev.* **2014**, *114*, 9487.
- [68] A. Van der Ven, J. Bhattacharya, A. A. Belak, *Acc. Chem. Res.* **2013**, *46*, 1216.
- [69] M. Wagemaker, F. M. Mulder, *Acc. Chem. Res.* **2013**, *46*, 1206.
- [70] J. Li, W. Wan, H. Zhou, J. Li, D. Xu, *Chem. Commun.* **2011**, *47*, 3439.
- [71] B. Liu, D. Deng, J. Y. Lee, E. S. Aydil, *J. Mater. Res.* **2010**, *25*, 1588.
- [72] Z. Guo, X. Dong, D. Zhou, Y. Du, Y. Wang, Y. Xia, *RSC Adv.* **2013**, *3*, 3352.
- [73] C. W. Mason, I. Yeo, K. Saravanan, P. Balaya, *RSC Adv.* **2013**, *3*, 2935.
- [74] W. Zhuang, L. Lu, X. Wu, W. Jin, M. Meng, Y. Zhu, X. Lu, *Electrochem. Commun.* **2013**, *27*, 124.
- [75] S.-T. Myung, N. Takahashi, S. Komaba, C. S. Yoon, Y.-K. Sun, K. Amine, H. Yashiro, *Adv. Funct. Mater.* **2011**, *21*, 3231.
- [76] Z. Yang, G. Du, Z. Guo, X. Yu, Z. Chen, T. Guo, H. Liu, *J. Mater. Chem.* **2011**, *21*, 8591.
- [77] J. Hou, R. Wu, P. Zhao, A. Chang, G. Ji, B. Gao, Q. Zhao, *Mater. Lett.* **2013**, *100*, 173.
- [78] X. Li, Y. Zhang, T. Li, Q. Zhong, H. Li, J. Huang, *J. Power Sources* **2014**, *268*, 372.
- [79] Z. Yang, G. Du, Q. Meng, Z. Guo, X. Yu, Z. Chen, T. Guo, R. Zeng, *RSC Adv.* **2011**, *1*, 1834.
- [80] D.-A. Zhang, Q. Wang, Q. Wang, J. Sun, L.-L. Xing, X.-Y. Xue, *Mater. Lett.* **2014**, *128*, 295.
- [81] W. Xiong, Y. D. Wang, H. Xia, *Mater. Technol.* **2013**, *28*, 260.
- [82] Z. Yang, G. Du, Z. Guo, X. Yu, Z. Chen, T. Guo, R. Zeng, *Nanoscale* **2011**, *3*, 4440.
- [83] A. R. Armstrong, C. Arrouvel, V. Gentili, S. C. Parker, M. S. Islam, P. G. Bruce, *Chem. Mater.* **2010**, *22*, 6426.
- [84] M. V. Koudriachova, *J. Nano Res.* **2010**, *11*, 159.
- [85] M. V. Koudriachova, *Surf. Interface Anal.* **2010**, *42*, 1330.
- [86] Y. Tang, Y. Zhang, J. Deng, J. Wei, H. L. Tam, B. K. Chandran, Z. Dong, Z. Chen, X. Chen, *Adv. Mater.* **2014**, *26*, 6111.
- [87] S. Brutti, V. Gentili, H. Menard, B. Scrosati, P. G. Bruce, *Adv. Energy Mater.* **2012**, *2*, 322.
- [88] J. Qu, Q.-D. Wu, Y.-R. Ren, Z. Su, C. Lai, J.-N. Ding, *Chem.: Asian J.* **2012**, *7*, 2516.
- [89] X. Li, Y. Zhang, Q. Zhong, T. Li, H. Li, J. Huang, *Appl. Surf. Sci.* **2014**, *313*, 877.
- [90] J. Qu, J. E. Cloud, Y. Yang, J. Ding, N. Yuan, *ACS Appl. Mater. Interfaces* **2014**, *6*, 22199.
- [91] S. K. Das, A. J. Bhattacharyya, *Mater. Chem. Phys.* **2011**, *130*, 569.
- [92] Y. Li, Z. Wang, X.-J. Lv, *J. Mater. Chem. A* **2014**, *2*, 15473.
- [93] M. Saito, Y. Nakano, M. Takagi, N. Honda, A. Tasaka, M. Inaba, *J. Power Sources* **2013**, *244*, 50.
- [94] B.-R. Kim, K.-S. Yun, H.-J. Jung, S.-T. Myung, S.-C. Jung, W. Kang, S.-J. Kim, *Curr. Appl. Phys.* **2013**, *13*, S148.
- [95] M. Fehse, F. Fischer, C. Tessier, L. Stievano, L. Monconduit, *J. Power Sources* **2013**, *231*, 23.
- [96] Y. Ishii, K. Okamura, T. Matsushita, S. Kawasaki, *Mater. Express* **2012**, *2*, 23.
- [97] C. Chen, X. Hu, P. Hu, Y. Qiao, L. Qie, Y. Huang, *Eur. J. Inorg. Chem.* **2013**, *2013*, 5320.
- [98] H. Huang, Z. Yu, W. Zhu, Y. Gan, Y. Xia, X. Tao, W. Zhang, *J. Phys. Chem. Solids* **2014**, *75*, 619.
- [99] H.-Y. Wu, M.-H. Hon, C.-Y. Kuan, I.-C. Leu, *J. Electron. Mater.* **2014**, *43*, 1048.
- [100] B.-R. Kim, K.-S. Yun, H.-J. Jung, S.-T. Myung, S.-C. Jung, W. Kang, S.-J. Kim, *Chem. Cent. J.* **2013**, *7*, 174.
- [101] L. Fernandez-Werner, R. Faccio, A. Juan, H. Pardo, B. Montenegro, A. W. Mombru, *Appl. Surf. Sci.* **2014**, *290*, 180.
- [102] H. Jang, S. Suzuki, M. Miyayama, *J. Power Sources* **2012**, *203*, 97.
- [103] H. Noguchi, S. Miyazaki, Y. Tanaka, W. Zhao, *Electrochemistry* **2012**, *80*, 787.
- [104] V. Etacheri, Y. Kuo, A. Van der Ven, B. M. Bartlett, *J. Mater. Chem. A* **2013**, *1*, 12028.
- [105] S. Liu, Z. Wang, C. Yu, H. B. Wu, G. Wang, Q. Dong, J. Qiu, A. Eychmüller, X. W. Lou, *Adv. Mater.* **2013**, *25*, 3462.
- [106] Z. Zhang, Q. Chu, H. Li, J. Hao, W. Yang, B. Lu, X. Ke, J. Li, J. Tang, *J. Colloid Interface Sci.* **2013**, *409*, 38.
- [107] H. Yu, J. Kong, R.-Y. Lai, *J. Struct. Chem.* **2013**, *32*, 1591.
- [108] C. Chen, X. Hu, Z. Wang, X. Xiong, P. Hu, Y. Liu, Y. Huang, *Carbon* **2014**, *69*, 302.
- [109] Z. Sun, X. Huang, M. Muhler, W. Schuhmann, E. Ventosa, *Chem. Commun.* **2014**, *50*, 5506.
- [110] P.-C. Chen, M.-C. Tsai, H.-C. Chen, I. N. Lin, H.-S. Sheu, Y.-S. Lin, J.-G. Duh, H.-T. Chiu, C.-Y. Lee, *J. Mater. Chem.* **2012**, *22*, 5349.
- [111] Z. Zhang, Z. Zhou, S. Nie, H. Wang, H. Peng, G. Li, K. Chen, *J. Power Sources* **2014**, *267*, 388.
- [112] V. Etacheri, J. E. Yourey, B. M. Bartlett, *ACS Nano* **2014**, *8*, 1491.
- [113] T. M. Breault, B. M. Bartlett, *J. Phys. Chem. C* **2012**, *116*, 5986.
- [114] J. Wang, Y. Zhou, Z. Shao, *Electrochim. Acta* **2013**, *97*, 386.
- [115] Z. Yan, L. Liu, J. Tan, Q. Zhou, Z. Huang, D. Xia, H. Shu, X. Yang, X. Wang, *J. Power Sources* **2014**, *269*, 37.
- [116] Y. Ishii, Y. Kanamori, T. Kawashita, I. Mukhopadhyay, S. Kawasaki, *J. Phys. Chem. Solids* **2010**, *71*, 511.
- [117] Y. Cai, B. Zhao, J. Wang, Z. Shao, *J. Power Sources* **2014**, *253*, 80.
- [118] N. D. Petkovich, S. G. Rudisill, B. E. Wilson, A. Mukherjee, A. Stein, *Inorg. Chem.* **2014**, *53*, 1100.
- [119] A. G. Dylla, J. A. Lee, K. J. Stevenson, *Langmuir* **2012**, *28*, 2897.
- [120] H. Liu, Z. Bi, X.-G. Sun, R. R. Unocic, M. P. Paranthaman, S. Dai, G. M. Brown, *Adv. Mater.* **2011**, *23*, 3450.
- [121] Y. Furuya, W. Zhao, T. Iida, M. Unno, H. Noguchi, *Electrochemistry* **2014**, *82*, 7.
- [122] N. Gunawardhana, Y. Ogumori, M. Yoshio, H. Nakamura, *Int. J. Electrochem. Sci.* **2014**, *9*, 6975.
- [123] C. Wessel, L. Zhao, S. Urban, R. Ostermann, I. Djerdj, B. M. Smarsly, L. Chen, Y.-S. Hu, S. Sallard, *Chem. -Eur. J.* **2011**, *17*, 775.
- [124] G.-N. Zhu, C.-X. Wang, Y.-Y. Xia, *J. Power Sources* **2011**, *196*, 2848.
- [125] Y. Furuya, W. Zhao, M. Unno, H. Noguchi, *Electrochim. Acta* **2014**, *136*, 266.
- [126] X. Wang, Y. Yan, B. Hao, G. Chen, *ACS Appl. Mater. Interfaces* **2013**, *5*, 3631.
- [127] Y. G. Andreev, P. M. Panchmatia, Z. Liu, S. C. Parker, M. S. Islam, P. G. Bruce, *J. Am. Chem. Soc.* **2014**, *136*, 6306.
- [128] A. S. Dalton, A. A. Belak, A. Van der Ven, *Chem. Mater.* **2012**, *24*, 1568.
- [129] A. G. Dylla, P. H. Xiao, G. Henkelman, K. J. Stevenson, *J. Phys. Chem. Lett.* **2012**, *3*, 2015.
- [130] Y. Tang, Y. Zhang, J. Deng, J. Wei, T. Hong Le, B. K. Chandran, Z. Dong, Z. Chen, X. Chen, *Adv. Mater.* **2014**, *26*, 6111.

- [131] Y. Tang, Y. Zhang, W. Li, B. Ma, X. Chen, *Chem. Soc. Rev.* **2015**, *44*, 5926.
- [132] Q.-W. Wang, X.-F. Du, X.-Z. Chen, Y.-L. Xu, *Acta. Phys. Sin.* **2015**, *31*, 1437.
- [133] J. Qi, X. Lai, J. Wang, H. Tang, H. Ren, Y. Yang, Q. Jin, L. Zhang, R. Yu, G. Ma, Z. Su, H. Zhao, D. Wang, *Chem. Soc. Rev.* **2015**, *44*, 6749.
- [134] X. Yan, Z. Wang, M. He, Z. Hou, T. Xia, G. Liu, X. Chen, *Energy Technol.* **2015**, *3*, 801.
- [135] B. Yuan, L. Cademartiri, *J. Mater. Sci. Technol.* **2015**, *31*, 607.
- [136] Y. Zhang, Z. Jiang, J. Huang, L. Y. Lim, W. Li, J. Deng, D. Gong, Y. Tang, Y. Lai, Z. Chen, *RSC Adv.* **2015**, *5*, 79479.
- [137] J. A. Dawson, J. Robertson, *J. Phys. Chem. C* **2016**, *120*, 22910.
- [138] Y. Zhang, Y. Tang, W. Li, X. Chen, *ChemNanoMat* **2016**, *2*, 764.
- [139] M. B. Vazquez-Santos, P. Tartaj, E. Morales, J. M. Amarilla, *Chem. Rec.* **2018**, *18*, 1178.
- [140] D. McNulty, A. Lonergan, S. O'Hanlon, C. O'Dwyer, *Solid State Ion* **2018**, *314*, 195.
- [141] Q. Zhang, Y. Wei, H. Yang, D. Su, Y. Ma, H. Li, T. Zhai, *ACS Appl. Mater. Interfaces* **2017**, *9*, 7009.
- [142] L. N. Cong, H. M. Xie, J. H. Li, *Adv. Energy Mater.* **2017**, *7*, 1601906.
- [143] Z. Bian, J. Zhu, H. Li, *J. Photochem. Photobiol. C: Photochem. Rev.* **2016**, *28*, 72.
- [144] A. W. Anwar, A. Majeed, N. Iqbal, W. Ullah, A. Shuaib, U. Ilyas, F. Bibi, H. M. Rafique, *J. Mater. Sci. Technol.* **2015**, *31*, 699.
- [145] S. Abu Bakar, C. Ribeiro, *J. Photochem. Photobiol. C: Photochem. Rev.* **2016**, *27*, 1.
- [146] G. E. Blomgren, *J. Electrochem. Soc.* **2017**, *164*, A5019.
- [147] L. Croguennec, M. R. Palacin, *J. Am. Chem. Soc.* **2015**, *137*, 3140.
- [148] F. Legrain, O. Malyi, S. Manzhos, *J. Power Sources* **2015**, *278*, 197.
- [149] J.-Y. Hwang, S.-T. Myung, Y.-K. Sun, *Chem. Soc. Rev.* **2017**, *46*, 3529.
- [150] J. Q. Deng, W. B. Luo, S. L. Chou, H. K. Liu, S. X. Dou, *Adv. Energy Mater.* **2018**, *8*, 1701428.
- [151] A. Vlad, N. Singh, C. Galande, P. M. Ajayan, *Adv. Energy Mater.* **2015**, *5*, 1402115.
- [152] V. Aravindan, Y.-S. Lee, R. Yazami, S. Madhavi, *Mater. Today* **2015**, *18*, 345.
- [153] J. Wang, J. Xie, Y. Jiang, J. Zhang, Y. Wang, Z. Zhou, *J. Mater. Sci.* **2015**, *50*, 6321.
- [154] L. Wu, D. Bresser, D. Buchholz, S. Passerini, *J. Electrochem. Soc.* **2015**, *162*, A3052.
- [155] Y. Tang, L. Hong, Q. Wu, J. Li, G. Hou, H. Cao, L. Wu, G. Zheng, *Electrochim. Acta* **2016**, *195*, 27.
- [156] Y. Liu, F. Zhao, J. Li, Y. Li, J. A. McLeod, L. Liu, *J. Mater. Chem. A* **2017**, *5*, 20005.
- [157] W. Zhang, Y. Zhang, L. Yu, N.-L. Wu, H. Huang, M. Wei, *J. Mater. Chem. A* **2019**, *7*, 3842.
- [158] W. Zhang, L. Cai, S. Cao, L. Qiao, Y. Zeng, Z. Zhu, Z. Lv, H. Xia, L. Zhong, H. Zhang, X. Ge, J. Wei, S. Xi, Y. Du, S. Li, X. Chen, *Adv. Mater.* **2019**, *31*, 1906156.
- [159] Y. Wang, J. Zhang, *Ionics* **2019**, *26*, 1159.
- [160] W. F. Zhang, Y. Zhang, L. Yu, N. L. Wu, H. T. Huang, M. D. Wei, *J. Mater. Chem. A* **2019**, *7*, 3842.
- [161] Y. Wang, J. Zhang, *Ionics* **2020**, *26*, 1159.
- [162] X. Yan, Y. Li, M. Li, Y. Jin, F. Du, G. Chen, Y. Wei, *J. Mater. Chem. A* **2015**, *3*, 4180.
- [163] J. D. Zhu, Y. Lu, C. Chen, Y. Q. Ge, S. Jasper, J. D. Leary, D. W. Li, M. J. Jiang, X. W. Zhang, *J. Alloys Compd.* **2016**, *672*, 79.
- [164] S. Goriparti, E. Miele, M. Prato, A. Scarpellini, S. Marras, S. Monaco, A. Toma, G. C. Messina, A. Alabastri, F. De Angelis, L. Manna, C. Capiglia, R. P. Zaccaria, *ACS Appl. Mater. Interfaces* **2015**, *7*, 25139.
- [165] Y. Zhang, Q. Fu, Q. Xu, X. Yan, R. Zhang, Z. Guo, F. Du, Y. Wei, D. Zhang, G. Chen, *Nanoscale* **2015**, *7*, 12215.
- [166] Y. Zhang, Y. Meng, K. Zhu, H. Qu, Y. Ju, Y. Gao, F. Du, B. Zou, G. Chen, Y. Wei, *ACS Appl. Mater. Interfaces* **2016**, *8*, 7957.
- [167] C. T. Campbell, C. H. Peden, *Science* **2005**, *309*, 713.
- [168] P. Yan, J. Zheng, Z.-K. Tang, A. Devaraj, G. Chen, K. Amine, J.-G. Zhang, L.-M. Liu, C. Wang, *Nat. Nanotechnol.* **2019**, *14*, 602.
- [169] M. Cao, L. Gao, X. Lv, Y. Shen, *J. Power Sources* **2017**, *350*, 87.
- [170] M. Cao, Y. Bu, X. Lv, X. Jiang, L. Wang, S. Dai, M. Wang, Y. Shen, *Appl. Surf. Sci.* **2018**, *435*, 641.
- [171] Q. Liu, H. Zhan, H. Zhu, H. Liu, Z. Sun, J. Bell, A. Bo, Y. Gu, *Nano Lett.* **2019**, *19*, 7742.
- [172] A. X. Zhou, Y. Liu, X. Z. Zhu, X. Y. Li, J. M. Yue, X. G. Ma, L. Gu, Y. S. Hu, H. Li, X. J. Huang, L. Q. Chen, L. M. Suo, *Energy Storage Mater.* **2021**, *42*, 438.
- [173] Y. Cai, H.-E. Wang, S.-Z. Huang, J. Jin, C. Wang, Y. Yu, Y. Li, B.-L. Su, *Sci. Rep.* **2015**, *5*, 11557.
- [174] L. Ding, J. Chen, B. Dong, Y. Xi, L. Shi, W. Liu, L. Cao, *Electrochim. Acta* **2016**, *200*, 97.
- [175] S. Mehraeen, A. Tasdemir, S. A. Gursel, A. Yurum, *Nanotechnology* **2018**, *29*, 255402.
- [176] X. Liu, Q. Sun, A. M. C. Ng, A. B. Djuricic, M. Xie, C. Liao, K. Shih, M. Vranjes, J. M. Nedeljkovic, Z. Deng, *Nanotechnology* **2015**, *26*, 425403.
- [177] J. Zheng, D. Ma, X. Wu, P. Dou, Z. Cao, C. Wang, X. Xu, *J. Mater. Sci.* **2017**, *52*, 3016.
- [178] J. Li, D. Yang, X. Zhu, L. Wang, A. Umar, G. Song, *Sci. Adv. Mater.* **2015**, *7*, 821.
- [179] B. Chen, Y. Meng, F. Xie, F. He, C. He, K. Davey, N. Zhao, S.-Z. Qiao, *Adv. Mater.* **2018**, *30*, 1804116.
- [180] D. P. Opra, S. V. Gnedenkova, A. A. Sokolov, A. B. Podgorbunsky, A. Y. Ustinov, V. Y. Mayorov, V. G. Kuryavyi, S. L. Sinebryukhov, *J. Mater. Sci. Technol.* **2020**, *54*, 181.
- [181] Z. Y. Zhang, T. S. Hu, Q. M. Sun, Y. Chen, Q. X. Yang, Y. M. Li, *J. Power Sources* **2020**, *453*, 227908.
- [182] Y. Tang, Y. Zhang, O. I. Malyi, N. Bucher, H. Xia, S. Xi, Z. Zhu, Z. Lv, W. Li, J. Wei, M. Srinivasan, A. Borgna, M. Antonietti, Y. Du, X. Chen, *Adv. Mater.* **2018**, *30*, 1802200.
- [183] N. Takami, Y. Harada, T. Iwasaki, K. Hoshina, Y. Yoshida, *J. Power Sources* **2015**, *273*, 923.
- [184] S. Wang, D. Qu, Y. Jiang, W.-S. Xiong, H.-Q. Sang, R.-X. He, Q. Tai, B. Chen, Y. Liu, X.-Z. Zhao, *ACS Appl. Mater. Interfaces* **2016**, *8*, 20040.
- [185] T. Shen, X. Zhou, H. Cao, C. Zheng, Z. Liu, *RSC Adv.* **2015**, *5*, 22449.
- [186] M. Zhen, S. Guo, G. Gao, Z. Zhou, L. Liu, *Chem. Commun.* **2015**, *51*, 507.
- [187] Y. Yang, S. Liao, W. Shi, Y. Wu, R. Zhang, S. Leng, *RSC Adv.* **2017**, *7*, 10885.
- [188] N. M. Ncube, H. T. Zheng, *Mater. Res. Express* **2020**, *7*, 015504.
- [189] C. Cai, M. Y. Song, Q. X. Ou, J. M. Li, C. S. An, *J. Mater. Sci.: Mater. Electron.* **2021**, *32*, 18581.
- [190] D. P. Opra, S. V. Gnedenkova, S. L. Sinebryukhov, A. V. Gerasimenko, A. M. Ziatdinov, A. A. Sokolov, A. B. Podgorbunsky, A. Y. Ustinov, V. G. Kuryavyi, V. Y. Mayorov, I. A. Tkachenko, V. I. Sergienko, *Nanomaterials* **2021**, *11*, 1703.
- [191] Q. Wang, L. Shen, T. Xue, G. Cheng, C. Z. Huang, H. J. Fan, Y. P. Feng, *Adv. Funct. Mater.* **2021**, *31*, 2002187.
- [192] S. Liu, J. Yu, M. Jaroniec, *Chem. Mater.* **2011**, *23*, 4085.
- [193] X.-L. Cheng, M. Hu, R. Huang, J.-S. Jiang, *ACS Appl. Mater. Interfaces* **2014**, *6*, 19176.
- [194] L. Ni, R. Wang, Y. Fu, H. Wang, W. Liu, L. Zhu, S. Qiu, Z. Zhang, *J. Alloys Compd.* **2019**, *790*, 683.
- [195] D. P. Opra, S. V. Gnedenkova, S. L. Sinebryukhov, *J. Power Sources* **2019**, *442*, 227225.
- [196] T. Yoshida, D. Takimoto, D. Mochizuki, W. Sugimoto, *Electrochemistry* **2020**, *88*, 305.

- [197] X. Li, G. Wu, X. Liu, W. Li, M. Li, *Nano Energy* **2017**, 31, 1.
- [198] C. Chen, B. Zhang, L. Miao, M. Yan, L. Mai, Y. Huang, X. Hu, *J. Mater. Chem. A* **2016**, 4, 8172.
- [199] Z. S. Han, J. Peng, L. Liu, G. Wang, F. Yu, X. H. Guo, *RSC Adv.* **2017**, 7, 7864.
- [200] J. Liang, X. Zhang, X. Zhai, L. Zhang, W. Wu, K. Yu, *RSC Adv.* **2017**, 7, 53097.
- [201] C. Chen, Y. Mei, Y. Huang, X. Hu, *Mater. Res. Bull.* **2017**, 96, 365.
- [202] C. Wang, F. Wang, Y. Zhao, Y. Li, Q. Yue, Y. Liu, Y. Liu, A. A. Elzatahy, A. Al-Enizi, Y. Wu, Y. Deng, D. Zhao, *Nano Res.* **2016**, 9, 165.
- [203] G. Ren, M. N. F. Hoque, J. Liu, J. Warzywoda, Z. Fan, *Nano Energy* **2016**, 21, 162.
- [204] D. P. Opra, S. V. Gnedenkov, S. A. Sinebryukhov, A. Y. Ustinov, A. B. Podgorbunsky, A. A. Sokolov, *Russ. J. Inorg. Chem.* **2019**, 64, 680.
- [205] S. Y. Li, B. C. Church, *J. Appl. Electrochem.* **2017**, 47, 839.
- [206] H.-Y. Wu, M.-H. Hon, C.-Y. Kuan, I.-C. Leu, *Ceram. Int.* **2015**, 41, 9527.
- [207] J. Zhang, J. Shen, T. Wang, H. Zhang, C. Wei, K. Zhang, Y. Yue, *CrystEngComm* **2015**, 17, 1710.
- [208] Y. Zhou, Q. Zhu, J. Tian, F. Jiang, *Nanomaterials* **2017**, 7, 252.
- [209] X. Chen, Y. Huang, K. Zhang, X. Feng, M. Wang, *Electrochim. Acta* **2018**, 259, 131.
- [210] J. Zhang, Y. Li, T. Gao, X. Sun, P. Cao, G. Zhou, *Ceram. Int.* **2018**, 44, 8550.
- [211] S. Jiang, R. Wang, M. Pang, H. Wang, S. Zeng, X. Yue, L. Ni, Y. Yu, J. Dai, S. Qiu, Z. Zhang, *Electrochim. Acta* **2015**, 182, 406.
- [212] C. Chu, J. Yang, Q. Zhang, N. Wang, F. Niu, X. Xu, J. Yang, W. Fan, Y. Qian, *ACS Appl. Mater. Interfaces* **2017**, 9, 43648.
- [213] C. Chen, Y. Wen, X. Hu, X. Ji, M. Yan, L. Mai, P. Hu, B. Shan, Y. Huang, *Nat. Commun.* **2015**, 6, 7929.
- [214] Y. Li, J. Luo, X. Hu, X. Wang, J. Liang, K. Yu, *J. Alloys Compd.* **2015**, 651, 685.
- [215] J. Liang, X. Han, Y. Li, K. Ye, C. Hou, K. Yu, *New J. Chem.* **2015**, 39, 3145.
- [216] M. Zou, Z. Ma, Q. Wang, Y. Yang, S. Wu, L. Yang, S. Hu, W. Xu, P. Han, R. Zou, A. Cao, *J. Mater. Chem. A* **2016**, 4, 7398.
- [217] H. Ren, R. Yu, J. Qi, L. Zhang, Q. Jin, D. Wang, *Adv. Mater.* **2019**, 31, 1805754.
- [218] S. Gao, Y. Yan, G. Chen, *ACS Sustainable Chem. Eng.* **2016**, 4, 844.
- [219] X. Yan, Y. Wang, C. Liu, M. Guo, J. Tao, J. Cao, D. Fu, L. Dai, X. Yang, *J. Energy Chem.* **2018**, 27, 176.
- [220] J. Rong, M. Kun, X. Yu, Y. Zhang, *Int. J. Electrochem. Sci.* **2017**, 12, 11987.
- [221] M. Sondergaard, K. J. Dalgaard, E. D. Bojesen, K. Wonsyld, S. Dahl, B. B. Iversen, *J. Mater. Chem. A* **2015**, 3, 18667.
- [222] N. Zhou, Y. Wu, Q. Zhou, Y. Li, S. Liu, H. Zhang, Z. Zhou, M. Xia, *Appl. Surf. Sci.* **2019**, 486, 292.
- [223] X. Li, Y. Liu, X. Zhang, C. Yao, R. Wang, C. Xu, J. Lei, *Electrochim. Acta* **2019**, 298, 14.
- [224] J.-Y. Hwang, H.-L. Du, B.-N. Yun, M.-G. Jeong, J.-S. Kim, H. Kim, H.-G. Jung, Y.-K. Sun, *ACS Energy Lett.* **2019**, 4, 494.
- [225] X. Li, M. Li, J. Liang, X. Wang, K. Yu, *J. Alloys Compd.* **2016**, 681, 471.
- [226] L.-M. Kong, B.-L. Zhu, X.-Y. Pang, G.-C. Wang, *Acta. Phys. Sin.* **2016**, 32, 656.
- [227] F. M. Courtel, S. Niketic, D. Duguay, Y. Abu-Lebdeh, I. J. Davidson, *J. Power Sources* **2011**, 196, 2128.
- [228] X. Yan, Y. Zhang, K. Zhu, Y. Gao, D. Zhang, G. Chen, C. Wang, Y. Wei, *J. Power Sources* **2014**, 246, 95.



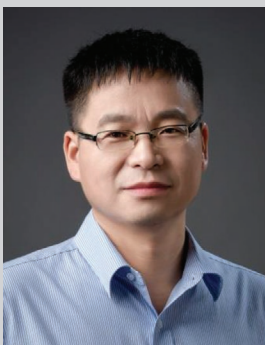
Suzhe Liang received his M.Sc. degree from the North University of China with a joint-supervision program at Ningbo Institute of Materials Technology and Engineering, Chinese Academy of Sciences. He is presently a Ph.D. candidate at the Institute for Functional Materials, Department of Physics, Technical University of Munich, Germany. His research interests involve anode materials for lithium/sodium-ion batteries and grazing incidence X-ray scattering techniques.



Xiaoyan Wang is a lecturer in the School of Materials and Chemical Engineering at the Ningbo University of Technology, China. She completed her postdoctoral research in the Institute of New Energy Technology in Ningbo Institute of Materials Technology and Engineering, Chinese Academy of Sciences, after receiving her Ph.D. in polymer chemistry and physics from the Chinese Academy of Sciences in 2019. Her research interests focus on metal oxide anode materials for lithium-ion batteries.



Ruoxuan Qi is currently a master student at the Ningbo Institute of Materials Technology and Engineering, Chinese Academy of Sciences. Her research interest focuses on interface studies in lithium secondary batteries.



Ya-Jun Cheng is a professor at the Institute of New Energy in Ningbo Institute of Material Technology and Engineering, Chinese Academy of Sciences. He received a B.S. degree from Peking University, China, followed by a Master degree from the University of Siegen, Germany, and completed his Ph.D. studies at the Max Planck Institute for Polymer Research in Mainz, Germany. From 2015 to 2017, he conducted research at the Department of Materials at the University of Oxford, sponsored by the Marie Skłodowska-Curie Fellowship from the EU. His research interests focus on polymer/inorganic nanohybrids for advanced battery applications.



Yonggao Xia is a professor at the Institute of New Energy Technology at Ningbo Institute of Materials Technology and Engineering, Chinese Academy of Sciences, heading the research group of Battery Green Design and Recycling Utilization. He received his Ph.D. in energy and materials science from Saga University, Japan, in 2008. His research interests focus on advanced materials and technologies for lithium-ion batteries.



Peter Müller-Buschbaum is a full professor in the Physics Department of the Technical University of Munich, Germany, heading the Chair of Functional Materials. Moreover, he is the scientific director of the Munich neutron source FRM II, scientific director of the Heinz Maier Leibnitz Zentrum MLZ, and heading the Bavarian key lab TUM.solar. His research interests cover polymer and hybrid materials for energy and sensing applications with a special focus on thin films and nanostructures, including kinetic, in situ, and operando experiments.



Xile Hu received a B.S. degree from Peking University (2000) and a Ph.D. degree from the University of California, San Diego (2004; advisor: Prof. Karsten Meyer). He carried out a post-doctoral study at the California Institute of Technology (advisor: Prof. Jonas Peters) before joining the faculty of the École Polytechnique Fédérale de Lausanne (EPFL) as a tenure-track assistant professor in 2007. He was promoted to associate professor in January 2013 and full professor in June 2016. He directs an interdisciplinary research program to develop catalysis for sustainable synthesis of added-value chemicals and cost-effective production of solar and electric fuels.